THE PENNSYLVANIA STATE UNIVERSITY
SCHREYER HONORS COLLEGE

DEPARTMENT OF BIOMEDICAL ENGINEERING

EXPERIMENTAL PLATFORM SIMULATING THE MECHANICAL EFFECTS OF DIAPHRAGMATIC MOTION ON INFERIOR VENA CAVA COLLAPSIBILITY

PHILIP CROMPTON
SPRING 2018

A thesis
submitted in partial fulfillment
of the requirements
for baccalaureate degrees
in Biomedical Engineering and Mechanical Engineering
with honors in Biomedical Engineering

Reviewed and approved* by the following:

Keefe B. Manning
Professor of Biomedical Engineering and Surgery
Thesis Supervisor

Justin L. Brown
Associate Professor of Biomedical Engineering
Honors Adviser

Peter J. Butler
Professor of Biomedical Engineering
Thesis Reader

* Signatures are on file in the Schreyer Honors College.

ABSTRACT

Recurrent pulmonary embolism (PE) is common with an annual 300,000-600,000 cases in the United States and is often preventatively treated with inferior vena cava (IVC) filters when patients are ineligible for anticoagulant therapy. IVC filters have been plagued with issues, including fracture and migration of filter parts, puncture of the vessel wall, and further thrombogenesis, all of which are intuitively impacted by filter hemodynamics. While several experimental and computational studies have been performed on filter hemodynamics, none of taken into account the effects of diaphragmatic compression during breathing on the IVC.

The goal of this study is to simulate the dynamic effects of diaphragmatic motion on IVC collapse experimentally, with validation provided through a computational model. To this end, a silicone model of typical IVC dimensions between the renal and iliac veins was placed in an acrylic chamber. A rigid track carrying a roller was placed on this chamber. Two stepper motors enabled the roller move in two dimensions, both compressing the vessel to an appropriate IVC collapsibility index (cIVC) and moving along its length for an appropriate total diaphragmatic excursion (TDE). Four conditions analogous to rest (2.0 lpm, 12 breaths/min, 15 % cIVC), light exercise (4.3 lpm, 16 breaths/min, 40% cIVC), heavy exercise (6.5 lpm, 20 breaths/min, 75% cIVC), and Valsalva maneuver (2.0 lpm, stationary, 30% cIVC) were tested. Additionally, a computational study was performed on a straight section of IVC with a stationary "roller" centered at a single point under the same conditions.

IVC elliptical cross-section axes were measured for five data sets at each condition to ensure repeatability and major axis strain values calculated under minor axis compression in both experimental and computational results. Similar trends and low percent differences were found between the experimental and computational data, suggesting partial validation of the experimental platform and supporting its ability to reproduce *in vivo* IVC geometric deformations for future studies of IVC filter performance and hemodynamics.

TABLE OF CONTENTS

LIST OF FIGURES

LIST OF TABLES

ACKNOWLEDGEMENTS

I would first like to thank my research and thesis advisor Dr. Keefe Manning for his constant support and encouragement throughout my three years of research at Penn State. Without his extraordinary patience and guidance, I never would have been able to finish this or any other project. His dedication to completing new research and to providing research opportunities to his students has opened up countless doors for my future.

I would also like to thank all of the other members of the Artificial Heart Laboratory. Their willingness to both assist and befriend the many other students in their lab has made my time in lab that much more enjoyable and successful. I would especially like to thank Bryan Good and Sailahari Ponnaluri for acting as mentors through my entire time in research, answering the smallest of questions and taking many hours out of their busy days to help me push forward with my own projects. The same thanks goes to all of the BME faculty and professors who have assisted me along the way, including my honors advisor Dr. Justin Brown, my thesis reader Dr. Peter Butler, and Gene Gerber, who played an enormous role in bringing my research ideas to life.

Last, I would like to thank my family and friends, especially my parents, Mary and Ed, and my brothers, Dan and Greg. Their unwavering encouragement and support throughout the years has been the inspiration for me to follow this path through thick and thin, and I would never be where I am today without them. Thank you.

Chapter 1

Deep Vein Thrombosis and Pulmonary Embolism

When a thrombus forms in one part of the body and travels through the blood vessels to another region, it is referred to as a thromboembolus[1]. More specifically, it is referred to as a pulmonary embolism when it travels to the lungs from any part of the venous system, where it causes damage by restricting or entirely blocking blood through a portion of the pulmonary circulation. While exact statistics for the prevalence of this condition are unknown, estimates predict that somewhere between 300,000 to 600,000 patients in the United States suffer from pulmonary embolism (PE) and the resulting complications every year. In about 30% of these affected patients, the damage caused by PE can result in death, often within hours of the clot dislodging and travelling to the lungs, making this a serious medical condition requiring active treatment. The most common cause of PE is from deep vein thrombosis (DVT), or the clotting of blood in the deep venous system[2]. In some situations, these clots can dislodge and travel through the venous system to the pulmonary circulation.

Section 1.1: Pathology of deep vein thrombosis

Deep vein thrombosis most commonly occurs in the deep veins of the calf and thigh. Most thrombi that cause pulmonary embolism form in the superficial femoral and popliteal veins of the thighs, as depicted in the magnetic resonance image in Figure 1-1. Here, the arrow highlights a large thrombus that has formed and remains attached to the wall of the popliteal vein.

Figure 1-1. Magnetic resonance direct thrombus imaging of showing thrombus development in the popliteal vein (adapted from Tan, 2014)[3]

Less frequently, DVT can occur in the posterior tibial and peroneal veins in the calf[2]. While this case is less likely to embolize directly to the pulmonary arteries, these clots can progressively embolize, shifting into the thigh and then subsequently towards the pulmonary arteries by means of the inferior vena cava.

DVT is mostly caused by two parts of Virchow's triad: abnormal hemodynamics leading to stagnant of sluggish venous return and damage to the endothelial lining of a blood vessel[4,5]. Either of these causes can stem from a variety of factors, including drug interactions or hormone therapies like birth control, injuries to the lower extremities that damages veins, and, most commonly, immobilization of a patient. About 50% of blood clots in patients form during or immediately following a hospital stay, when a patient may be confined to their bed or have had a medical procedure limiting their mobility, such as placing a cast or receiving major surgery.

Perhaps the largest contributor to DVT from Virchow's Triad is blood stasis in the venous system[5]. In this case, immobilization is the primary concern, and when a patient has limited physical

activity due to hospitalization, surgery, paralysis, or long travel, to name a few reasons, venous return can be significantly hindered, leading to more sluggish flow in the veins. Additionally, adequate blood perfusion through the lower extremities relies heavily on muscular contraction and respiratory inspiration to act as pumps aiding in venous return to the heart against gravity[6]. In the lower extremities, these pumps take the form of unidirectional venous valves[7] as illustrated in Figure 1-2.

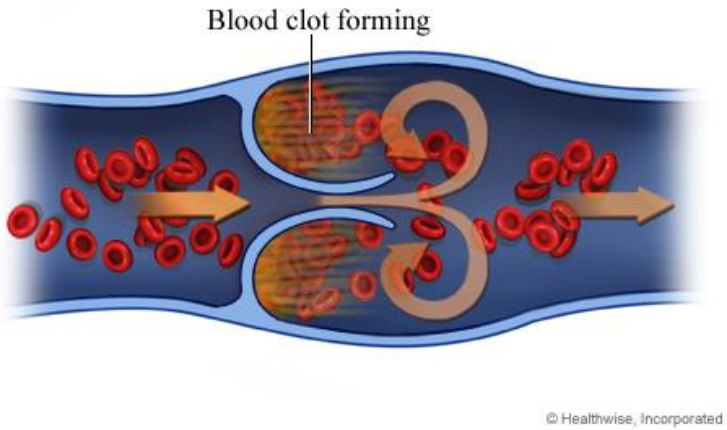

Figure 1-2. Thrombus formation resulting from recirculation patterns behind venous valve leaflets (adapted from Thompson, 2015)[6]

These valves act by restricting reverse flow, which can cause unusual flow profiles to develop, leading to recirculation and stagnation of blood behind the leaflets created by the shape of the valve[8]. In some studies of autopsies, thrombi have been found in these pockets created by venous valves, and the valves and surrounding veins were often enlarged. Especially in these valve pockets, but also in any region of reduced flow, procoagulants from the coagulation cascade can accumulate over time[7]. Combined with low shear rates, these factors can greatly increase the likelihood of deep vein thrombosis.

As another vertex of Virchow's Triad, damage to the endothelial cells can greatly increase the risk of thrombosis near the injury[5]. From a biochemistry perspective, the coagulation cascade plays a dominant role in this type of thrombogenesis and is comprised of several complex interactions between chemical pathways that can be activated, among other things, by an injury[9]. Normally, the endothelial lining expresses several anticoagulant factors, but an injury can diminish the cells' expression of these

proteins, thus triggering the coagulation cascade, which leads to platelet activation and the eventual formation of a thrombus at the site of the injury. While the specifics of this pathway are not important, it does provide an effective explanation for DVT following a serious injury to the lower extremities like surgery or a bone fracture.

A combination of both blood stasis due to immobilization and endothelial injury from wounds or surgeries is common in hospital settings, making DVT a serious issue during clinical care[10]. Overall, DVT affects about 1 in 1000 patients on a yearly basis but is not exclusively limited to immobilized patients. Other factors like age and pregnancy can also increase an individual's chance of developing a DVT. One study found that 1 out of 10,000 individuals aged 20-24 years have been affected by DVT compared to about 2 out of 1,000 for individuals aged 74-80, with a mean age of 61.7 years at the first incident.

Section 1.2: Relationship to pulmonary embolism

Without becoming dislodged, a deep vein thrombus can still cause serious symptoms, including chronic venous insufficiency, which can result in painful, reddish swelling of the region in the leg around the clot and the development of venous stasis ulcers[11]. This form of DVT and its symptoms are typically easy to treat with anticoagulants, but not all of these clots remain in the lower extremities; 50% of all deep vein thrombi eventually detach from the vessel wall and embolize[2] as shown in Figure 1-3, travelling through the inferior vena cava, through the heart, and into the pulmonary arteries, causing a pulmonary embolism.

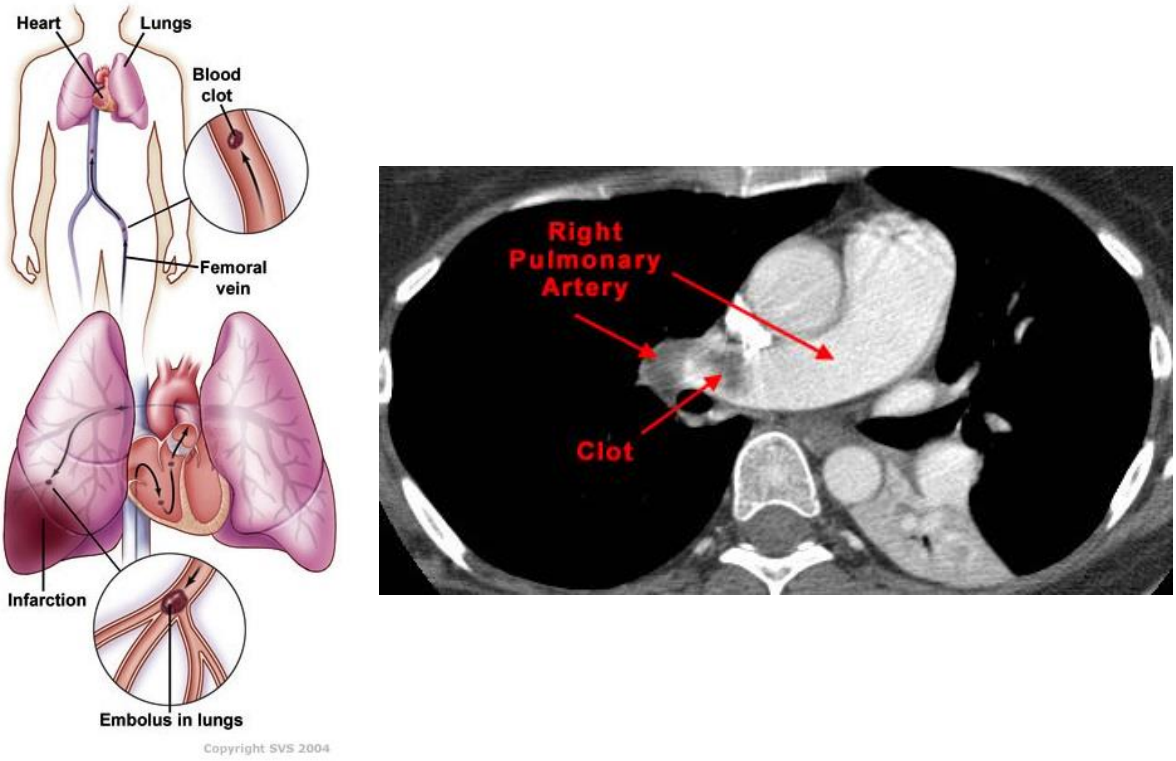

Figure 1-3. a) Dislodged thrombus path to PE (adapted from Avgerinos, 2004)[12] and b) CT scan showing large PE blocking right pulmonary artery (adapted from UVa, 2013)[13]

In one study of patients diagnosed PE, there was a 2.5% mortality rate caused directly by PE and a 24% mortality rate in diagnosed patients within one year of the first onset[14]. However, the actual number is likely higher for direct cases, as PE is fast acting[8]. The majority of deaths from PE occur within the first 2.5 hours of the venous thrombus dislodging from its location, so patients who fall into this category were completely unrepresented in this study[14], because a preliminary requirement was a diagnosis of the PE via a ventilation-perfusion lung scan. Estimates of the mortality rate associated with PE vary widely yet are always significantly large, with another study of 283 patients reporting a 15% mortality rate within three days of a hospitalizing diagnosis of PE[15].

Patients who do not experience a lethal PE event may experience several ongoing complications as a result. Even after successful treatment, 5-30% of patients have a recurrence of PE, with the likelihood of another event increasing with time[16]. Chronic thromboembolic pulmonary hypertension (CTEPH) also develops in 3.8% of patients in the two years following a PE event. Post-thrombotic

syndrome is especially common in PE cases originating from DVT, causing pain, swelling, ulcers, inflammation of the blood vessel, and an increased chance of thrombogenesis[4].

Section 1.3: Treatment and Prevention

The first step in treating DVT or PE has the fundamental goal of removing blood clots from the body with the least invasive procedures possible. To this end, anticoagulation therapy is normally a first choice after a diagnosis of DVT or PE[2]. Immediately following a diagnosis, short-term anticoagulation therapy starts with an initial injection of low molecular weight heparin during hospitalization. When heparin is only administered for a few days during the hospitalization of the patient, there is a 20% recurrence rate of DVT or PE[8], so long-term solutions are necessary in almost all cases. In order to minimize the amount of time a patient must spend undergoing active treatment in a hospital, it is more favorable to manage long-term anticoagulation therapy on an outpatient basis, so long term strategies are necessary. Oral doses of other anticoagulants, typically Vitamin-K antagonists like warfarin[2], can follow the initial heparin injection for an indefinite amount of time. Both heparin and Vitamin-K antagonist drugs attack the coagulation cascade responsible for the formation of these clots, albeit in different ways. Figure 1-4 pinpoints where each of these drugs target chemical pathways in the coagulation cascade at specific points to produce the desired response.

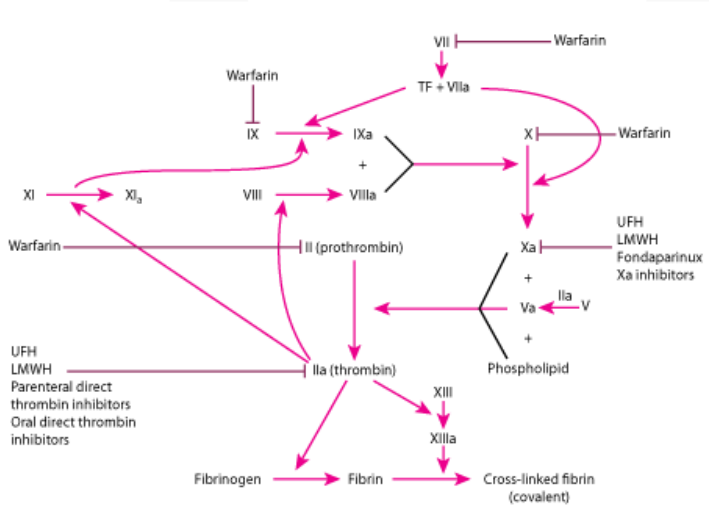

Figure 1-4. Coagulation cascade pathway depicting where multiple different anticoagulants inhibit the chemical pathway leading to thrombogenesis (UFH = unfractioned heparin, LMWH = low molecular weight heparin)[2]

Numerous recommendations exist regarding treatment duration. While most guidelines suggest 3-6 months[17] depending on the risk factors, some patients may have to take anticoagulants indefinitely if they have permanent risk factors such as genetic predispositions towards hypercoagulability or recurrent DVT/PE[2]. Sometimes, drug therapy is also combined with wearing compression stockings on the legs to encourage blood movement, preventing the formation of new clots[4].

Unfortunately, anticoagulation therapy can be ineffective or cause serious complications in a small number of patients. Drug therapies based both on heparin and Vitamin-K antagonists can result in major hemorrhage (5.0% of patients for heparins and 4.2% of patients per year for Warfarin)[8] as defined by a loss of greater than two units of blood in a week. In the case of heparins, thrombocytopenia (low blood platelet count) is also an issue to consider and can contribute to the possibility of major bleeding[2]. Some patients may be ineligible for anticoagulation therapy because of their pre-existing high risk of bleeding, a potential drug interaction with treatment from another illness, especially in cancer patients, or a failed anticoagulation treatment with recurrent hemorrhaging. Ultimately, anticoagulation therapies have sometimes proven ineffective in preventing the recurrence of DVT or PE without significant harm to the patient, provoking the development of alternative strategies for managing these diseases.

Chapter 2

Inferior Vena Cava Filters

Section 2.1: Inferior Vena Cava Filter Function and Development

When anticoagulation fails, physicians have turned to mechanical means of limiting the travel of blood clots in the body. As early as 1947, Homans attempted mechanical obstruction of the femoral vein, iliac vein, and even the inferior vena cava in order to prevent recurrent pulmonary embolism[18]. Obstructing a main blood vessel is a major surgery, and even he recognized that this was a last resort only, when all other available treatments had failed and another event would be fatal. Into the 1970s ligation of blood vessels remained a prevailing technique, but it drastically altered the venous return of blood to the heart, resulting in many complications[19]. Needing a less invasive method for obstructing the pathway of emboli in the inferior vena cava, Mobin-Uddin and McLean described the first primitive inferior vena cava filter in 1969 as an "umbrella filter" in the vessel[20], and they found that, despite added turbulence in blood flow and blockage of its openings, it still reduced potential fatalities from pulmonary embolism drastically[19].

Since then, many research groups and companies have iterated on this basic premise of a device that traps blood clots in venous blood flow. Figure 2-1 depicts several variations that have been developed, most of which trace their inspiration back to Mobin-Uddin and McLean's original umbrella shape.

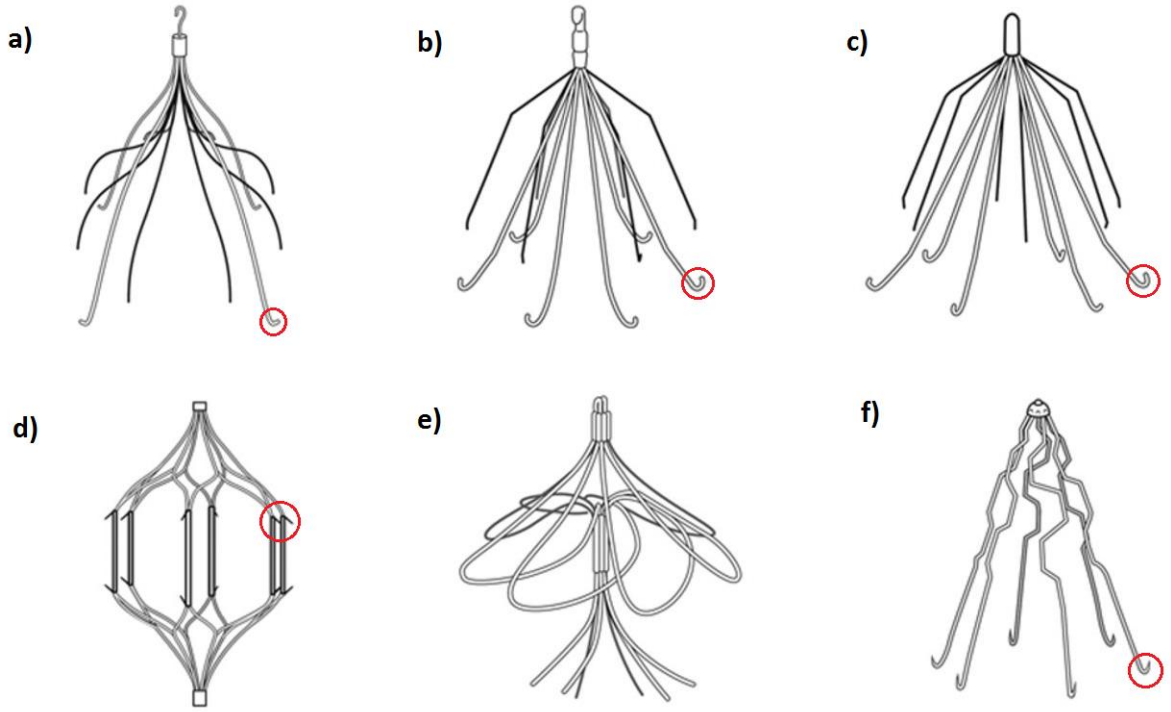

Figure 2-1. Some inferior vena cava filter models with anchoring hooks highlighted a) Celect filter (Cook, Bloomington, IN); b) Eclipse filter (Bard Peripheral, Tempe, AZ); c) G2 filter (Bard Peripheral, Tempe, AZ); d) TrapEase filter (Cordis, Milpitas, CA); e) Simon Nitinol filter (Bard Peripheral, Tempe, AZ); f) Greenfield filter (Boston Scientific, Marlborough, MA). (adapted from Jia, 2015)[21]

Each of these filter options vary in their vertical shape and wire profile perpendicular to the direction of blood flow, yet they all embody some key characteristics. First and foremost, nearly every filter shape is pyramidal in shape with thin, extended legs. These legs, when viewed from the direction of blood flow, create a wire mesh designed to catch thrombi travelling through the IVC towards the pulmonary circulation. In most cases, either these legs or the sides of the filter intended to make contact with the vessel wall have small hooks, as circled in Figure 2-1, meant to latch into the wall of the IVC so that the filter itself does not become dislodged.

As mentioned previously, IVC filters were designed as a less invasive alternative to surgery adding ligations to the main venous vessels, and they can be implanted through another part of the body[19]. Typically, these filters are made of a shape memory alloy that is easily collapsible onto a catheter, which

is then threaded through either the jugular or femoral vein[22]. The filter is guided using ultrasound to a region just between the renal and iliac veins then expanded to fill the entire cross-sectional area of the vessel[19].

IVC filters can be described as either permanent or temporary[22]. Since they are used as a measure of last resort when anticoagulation efforts fail, they are more often used in a permanent sense, where a patient will carry an implanted filter for the rest of their life. With their use becoming more common, some filters have been designed to be retrieved from the body once the risk of recurrent pulmonary embolism has subsided. Filters from across the design spectrum fall into both of these categories, but it is important to note that any filter labelled as temporary is also required to have the ability to endure as a permanent filter should it be needed.

Section 2.2: Issues Associated with Inferior Vena Cava Filters

As with their drug-based counterparts, IVC filters are far from a perfect treatment for pulmonary embolism, either proving ineffective or leading to their own complications. Because of their net-like structure, not every PE is necessarily caught by the filter if it is small enough to make it through the wire gaps[23]. In some studies, incident PE after the placement of a filter was up to 6.2% in patients that were already at high risk for PE, a decrease from recurrent PE occurring in 15.1% of high-risk patients who did not receive a filter.

Complications aside from filter ineffectiveness can also arise from any of the available models. Of all of these, the most common is the development on new thrombi on the downstream surface of the filter, where they are then free to detach and cause their own PE. Figure 2-2 demonstrates this issue, displaying an explanted IVC filter with the downstream surface coated in a layer of clotted blood. Since this thrombosed layer occurs on the downstream side of the filter, it has potential to detach from this surface and travel directly to the pulmonary circulation, circumventing the filter entirely.

Figure 2-2. Explanted IVC filter with residual external thrombus formation (adapted from Sildirogu, 2012)[24]

One randomized study also showed that the placement of a filter increased the development of further DVT in patients[23]. In the long term, the filters are also known to fail mechanically, with some trials reporting up to 13.5% fracture frequency[25]. While this particular study did not include migration, filter parts have been frequently observed to migrate up the IVC as far as to the right ventricle of the heart[26]. These broken pieces can become lodged in the vessel wall, often penetrating through it into surrounding organs. Additionally, 12.5% of patients experienced partial or total blockage of the IVC beyond what was expected in filter use, and 47.9% experienced penetration of the vena cava wall by the mounting barbs on the legs of the implanted filter[25]. On top of this, filters are frequently misplaced or improperly secured, increasing the likelihood of fracture and migration[23]. These statistics clearly show that serious complications involving IVC filter failure are fairly common.

Chapter 3

Blood Flow Around Inferior Vena Cava Filters

Section 3.1: Hemodynamics around Inferior Vena Cava Filters

When analyzing the complications caused by inferior vena cava filters, it is important to consider the blood flow patterns, or hemodynamics, in the vicinity and downstream of an implanted filter. With the complex geometries presented by any of these filter models, it is reasonable to expect that an IVC filter can significantly impact the flow patterns in the IVC, potentially further contributing to the complications mentioned in Section 2.2. Multiple research efforts have confirmed that IVC hemodynamics can be adversely manipulated with the placement of IVC filters.

Leask *et al.* investigated the hemodynamics associated with the Simon Nitinol filter (Bard Peripheral, Tempe, AZ, Figure 2-1-e) using an artificial IVC model under steady flow conditions and found significant changes in IVC flow patterns when an IVC filter was implanted, especially after it had trapped an embolus. Figure 3-1 reveals clear flow disturbances, including a disruption of the expected parabolic velocity profile and a large, prothrombitic stagnant region inside the filter itself. This stagnation region is most severe just above the trapped clot, but other regions of slow flow compared to the average flow velocity exist near the tip of the filter and continue downstream. Along with this, turbulent regions were observed downstream[27]. Lastly, Leask *et al.* reported large changes in wall shear stress around the struts of the filter.

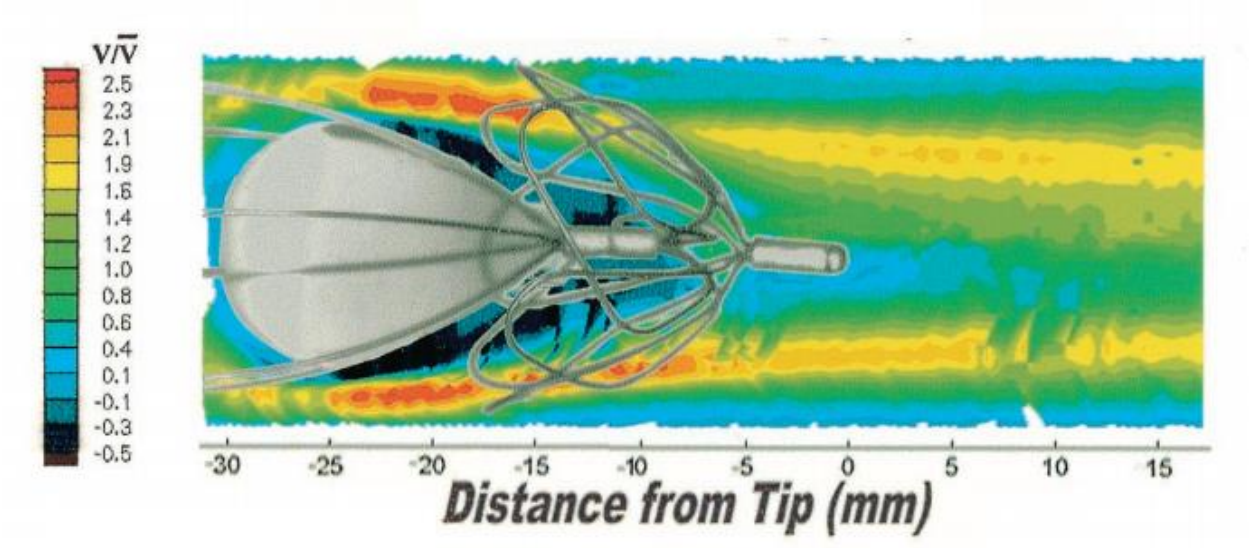

Figure 3-1. Visualized flow around a Simon Nitinol Filter revealing stagnation regions and downstream disruption of parabolic velocity profile (Bard Peripheral, Tempe, Az)[27]

Couch *et al.* pursued similar research and used photochronic flow visualization to look into flow changes surrounding Greenfield (Boston Scientific, Marlborough, MA, Figure 2-1-f) and VenaTech LGM (B. Braun Medical, Bethlehem, PA) filters mounted in a IVC flow model[28] and concluded that, despite differences between the magnitudes of effect in each filter, both did demonstrably alter the surrounding flow field, forming regions past the filter tip with velocities less than theoretically predicted in more than 50% of the vena cava. The team especially noted the flow disturbances caused by the cross-sectional shape of the filter struts, as shown in Figure 3-2. Both strut shapes in Figure 3-2 cause flow separation, which acted as trip wires that induced unnecessary turbulence in the flow field and caused small regions of recirculation in the "shadow" of the strut.

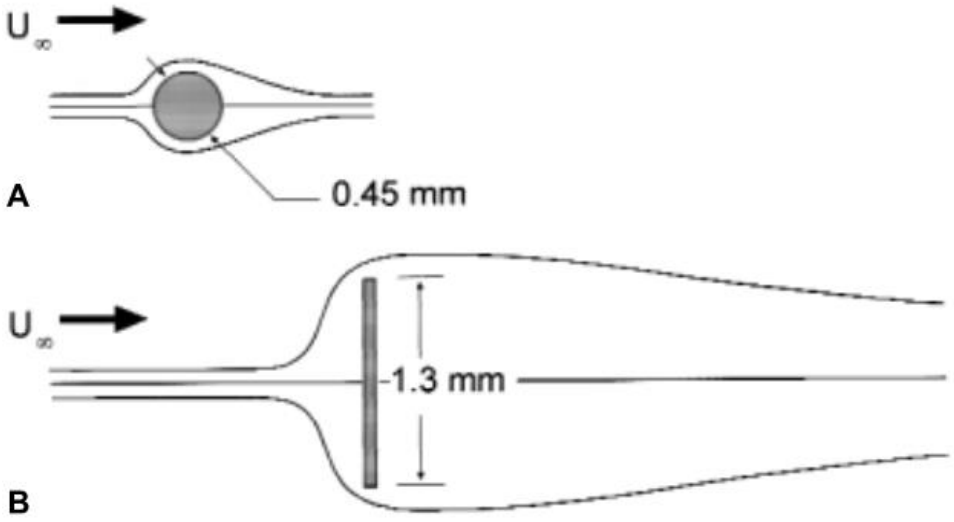

Figure 3-2. Flow disturbances downstream of a) round and b) flat filter struts (adapted from Couch *et al*, 2000)[28]

In addition to these *in vitro* studies, a large body of work on computational fluid dynamics (CFD) around IVC filters has been performed, yielding similar results. In one such study, a CFD simulation was performed on a Celect filter (Cook Medical, Bloomington, IN)[29]. In this study, a filter was simulated both with and without a trapped embolus in straight and tilted positions in order to investigate how faulty implantation or filter shift can contribute to adverse flow effects. The study observed worsening stagnation regions near the tip of the filter and the downstream edge of a trapped embolus as the filter increased in tilt, as illustrated by Figure 3-3. As discussed in Section 2.2, IVC filters frequently have issues with movement or are often implanted incorrectly, and this study only serves to highlight deteriorating flow conditions as the filter fails. As with other studies, this CFD simulation calculated elevated WSS in the vicinity of the filter.

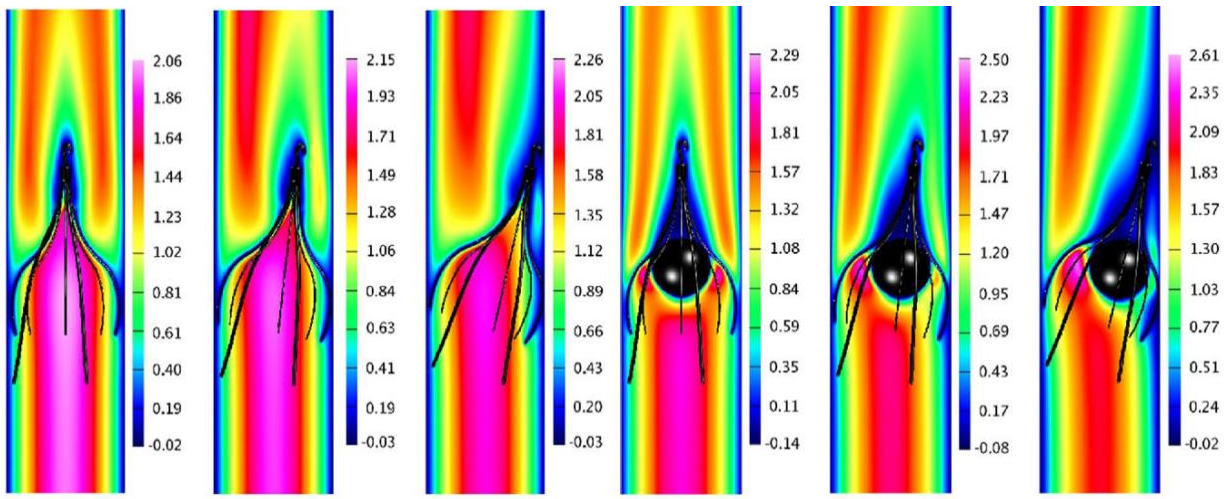

Figure 3-3. Axial velocity contours at various degrees of tilt with and without a captured embolus (adapted from Singer, 2011)[29]

In another, two patient specific IVC models were generated from CT scans and used as a basis for a computational study[30]. These IVC models and a G2 Express filter (Bard Peripheral, Tempe, AZ) were meshed and simulated under four cases corresponding to the IVC alone, the IVC with an implanted filter, the IVC with an implanted filter and trapped clot, and the IVC with an implanted filter and trapped clot under exercise conditions. Figure 3-4 summarizes the simulated results with axial velocity distributions in the frontal plane of the IVC for all four cases in both of the patient specific models. As noted by the team in their work, the presence of an IVC filter negatively impacted IVC flow in several ways. As in the other studies mentioned, stagnant recirculation regions formed near both the tip of the filter and the downstream side of the trapped embolus. In both models, filter placement resulted in lower near wall flow velocities and higher maximum flow velocities in the portions of the IVC that remained unobstructed.

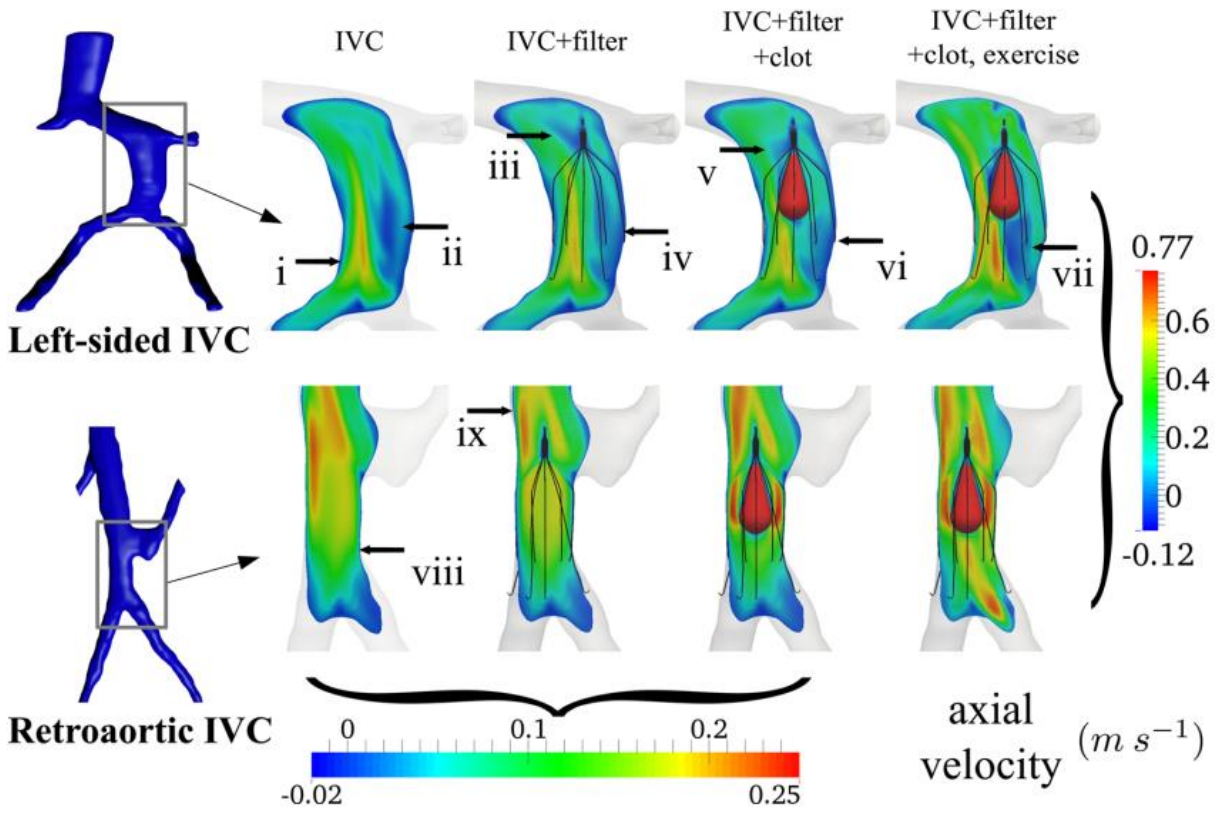

Figure 3-4. CFD velocity profiles around IVC filters under four test conditions for two patient-specific IVC models (adapted from Aycock *et al*, 2014)[30]

Additionally, the team calculated wall shear stress (WSS) values on the surface of the IVC filter and its trapped embolus and found that the presence of the embolus drastically increased the magnitude of surface stresses on the modeled filter.

Section 3.2: Diaphragmatic Motion and the Inferior Vena Cava

Combined with an increased likelihood of thrombogenesis, altered flow patterns like elevated WSS on the filter surface could mechanically affect the structure, potentially fracturing it and allowing its struts to migrate downstream, causing serious complications. Another large factor influencing the flow inside of the IVC when a filter is present is the diaphragmatic motion compressing the IVC between the iliac and renal veins. In the course of its motion, the diaphragm moves periodically between these two

regions, compressing the IVC as it does so[31]. For clarification on this cross-sectional compression, Figure 3-5 provides a typical ultrasound recording in a patient performing a Valsalva maneuver (attempted forced expiration with mouth and nose sealed). Similar compression occurs during normal breathing as well.

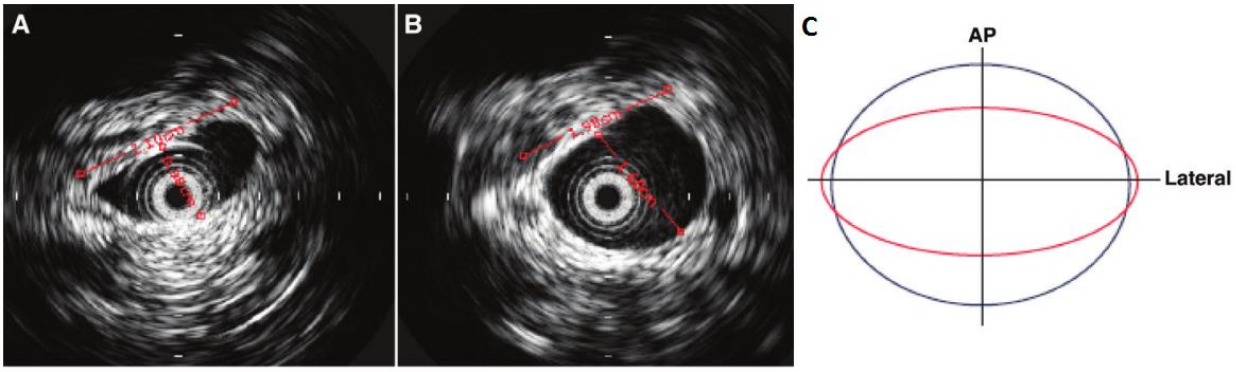

Figure 3-5. a) Minimum and b) maximum IVC diameters during a Valsalva maneuver and c) a simplified cross-section showing typical compression (adapted from Murphy, 2008)[31]

In order to quantify this compression, the IVC collapsibility index is a widely used diagnostic tool describing the compression of the IVC and is defined as[32]:

$$cIVC\ \% = \frac{D_{max} - D_{min}}{D_{max}} \times 100\%$$

where D_{max} and D_{min} describe the maximum and minimum diameters of the inferior vena cava during a respiratory cycle, measured across the sagittal plane. In a normal patient, this index can take any value from 0 to 100%, depending on the forcefulness of respiration (due to exercise, Valsalva maneuver, etc.)[33]. As a result, the hemodynamics in this area are likely to change dynamically throughout any given respiratory cycle. Figure 3-6 gives a representation of the geometric variation in the vena cava under increasing diaphragmatic excursion at "low, moderate, and high inspiratory effort", clearly showing how the IVC diameter changes in response to diaphragmatic excursion (full range of diaphragmatic motion during a breath).

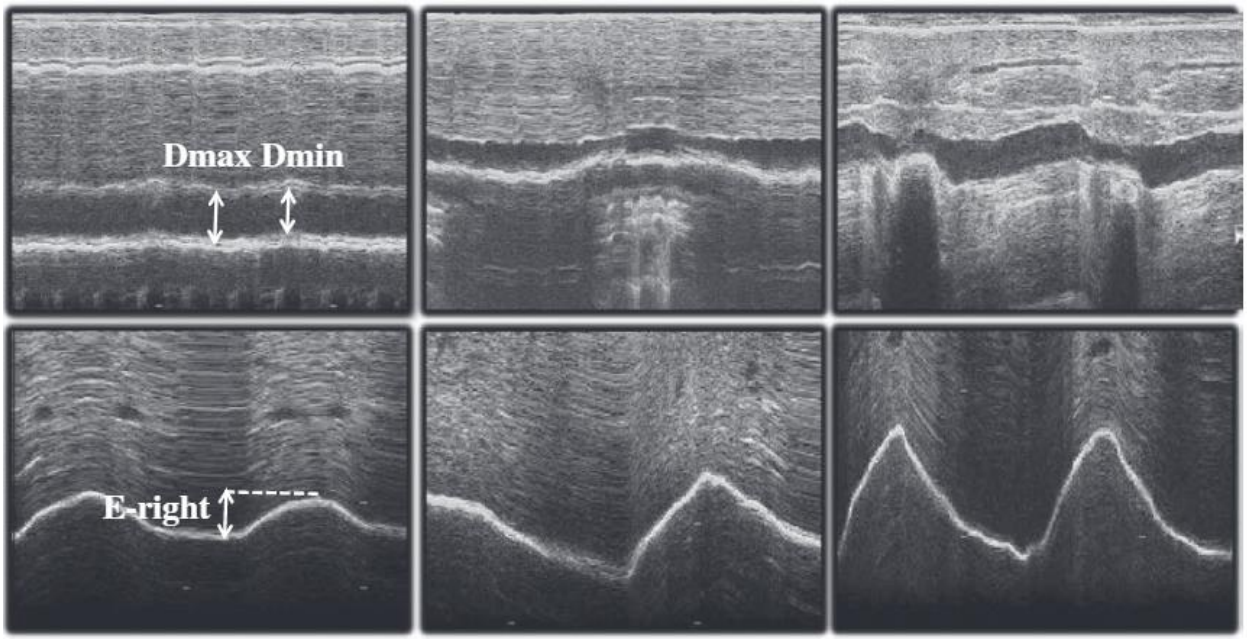

Figure 3-6. Echographic recordings of inferior vena cava diameter (top) and diaphragmatic excursion (bottom) under low (left), moderate (center), and high (right) inspiratory effort (adapted from Gignon, 2016)[33]

The compression in Figure 3-6 occurs in the region of the IVC between the renal and iliac veins, the exact location in which IVC filters are implanted. Blood enters this region from either the lower extremities via the iliac veins or from the kidneys via the renal veins and flows towards the heart in a steady process. While this occurs, the diaphragm periodically moves between the iliac and renal veins, compressing local sections of the IVC as it moves. Here, the IVC is a low pressure and compliant vessel, especially when compared to the rigidity of the muscle making up the diaphragm. Therefore, this diaphragmatic movement changes the wall geometry of the IVC as it passes, which intuitively affects hemodynamics around an implanted filter and the mechanical forces to which the filter is subjected.

To date, only one known study has been conducted by Laborda *et al.* taking into account the diaphragmatic motion to investigate IVC filter performance[34]. In it, patients with implanted IVC filters were monitored during tidal breathing and a requested Valsalva maneuver, and it was found that patients performing the Valsalva maneuver were more likely to experience filter complications, specifically IVC wall penetration in this case.

Tedaldi *et al.* explored the specific hemodynamics within the IVC during compression[35]. This team performed an experimental and computational study side by side of a compressed IVC model, and found significant qualitative differences in the flow field, most notably redirection and further propagation of high velocity jets downstream from the iliac veins from venous inlets, especially under higher amounts of collapse. These high velocity jets were always accompanied by regions of recirculation, which became less uniform with higher collapse. Lastly, the team also noted increases in wall shear stress values with larger compression values. While this study is similar to the objective of this research, the team did not study the hemodynamics with a filter in place, and also limited the study to a static total compression of the entire IVC representing a Valsalva maneuver rather than the local, pronounced compression more specifically caused by diaphragmatic motion during breathing. Overall, both of these studies strongly indicate that diaphragmatic motion can be an influential factor on filter performance and merits further study.

Section 3.3: Study Objectives

The motivation for this study comes from a need to further quantify the effect of the previously mentioned diaphragmatic motion on the flow characteristics around an IVC filter. The geometry of the IVC, especially with an implanted filter, is incredibly complex from an analytic fluid mechanics standpoint. Combined with the dynamic effects of diaphragmatic motion on the cross-sectional geometry of the IVC, data must be collected experimentally in order to fully understand the affected flow regime.

The main goal of this study is to experimentally reproduce the geometric effects on the IVC *in vivo* that arise from dynamic IVC compression. To do so, an experimental platform will be created that can simulate localized compressive motion in several physiological states, including rest (tidal breathing), moderate exercise, heavy exercise, and during a Valsalva maneuver. Each of these states is characterized by specific ranges of cIVC values, breathing frequencies, ranges of diaphragmatic motion, and flow

conditions. This setup will take imaging abilities into consideration for future work in quantifying the IVC flow field around an implanted IVC filter during compression using particle image velocimetry (PIV).

In addition to an experimental setup, a computational study will be performed. While the experimental platform will focus on developing a substitute material model for the IVC, computational work will be performed on a model of the IVC in the infrarenal region. This study will mimic the conditions placed on an experimental IVC model in all states tested, with the ultimate goal of being used to validate the experimental platform.

Chapter 4

Experimental Platform Materials and Methods

Section 4.1: Inferior Vena Cava Model

A model of the inferior cava was manufactured partially using dimensional specifications from previous work in the lab by Evan Fox[36]. This model includes the portion of the IVC from renal to iliac veins and was modified to include smoother transitions between the iliac veins and IVC, preventing recirculation regions that were previously observed. The dimensions of the model were chosen to be anatomically correct and are given in Table 4-1. The length of the peripheral veins was chosen to be ten times their respective diameters to achieve fully developed flow entering the IVC.

Table 4-1. IVC model dimensions (adapted from Fox, 2013)[36]

Vessel	Length (mm)	Diameter (mm)
Inferior Vena Cava	200	28.8
Left Renal Vein	127	12.7
Right Renal Vein	93	9.3
Left/Right Iliac Vein	120	12.0

These dimensions were used to create a 3D model in SolidWorks. Special care was taken to ensure that the iliac to vena cava vessel transition was not abrupt. Figure 4-1 shows a solid rendering of the inner wall dimensions of the IVC model used, and Figure 4-2 includes the length dimensions of the model in a projected engineering drawing from the front side of the model. Note that the left and right sides of the model are labelled in both sets of drawings, along with a set of coordinate axes.

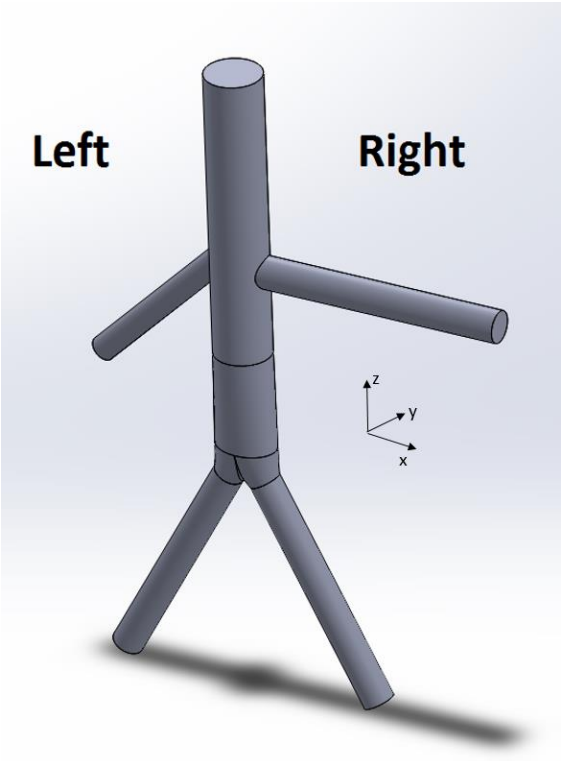

Figure 4-1. SolidWorks render of 3D IVC model with revised iliac junction reducing recirculation and coordinate axes

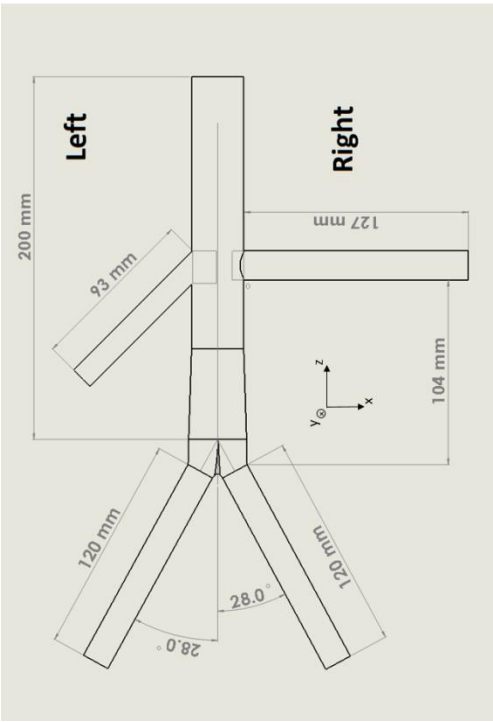

Figure 4-2. Length and angle specifications for IVC model with coordinate axes

Figures 4-1 and 4-2 also establish a coordinate system within the model. The simplest of these is the positive z-direction, which points along the center axis of the IVC in the direction of blood flow. The positive y-direction is then defined in the direction in which the IVC is compressed by diaphragmatic motion (see Figure 4-4), and the x-axis is defined perpendicular to both of these. The x and y-axes also fall in line with the major and minor axes of the IVC's elliptical cross-section. The major axis of the IVC's cross-section falls along the "horizontal" x-axis, and the minor axis of the IVC's cross-sections falls along the "vertical" y-axis.

The IVC models were created in house using a pseudo-casting process for silicone materials. For this purpose, two models of the IVC were 3D printed. One was an inner model, representing the hollow lumen area of the IVC with the above dimensions, and one was an outer model, scaled up to an outer wall size, giving an ultimate wall thickness of 1.0 mm.

Using the outer model, a silicone mold made of Eurosil 45 was created by pouring the still-liquid silicone into a molding box and allowing the material to set. Injection holes were then cut into the ends of the iliac veins and the downstream outlet of the vena cava. The two halves of the mold were then placed around the inner "lumen" model, which served as a "core" for the casting process. Sylgard 184 was then mixed and injected into the mold under a vacuum to create a shell modelling the vasculature of the IVC. Once set, the two halves of the mold were removed.

Sylgard 184 was chosen as an experimental material for two main reasons. First and most importantly, this silicone polymer is optically clear, with a refractive index that can easily be matched with a blood analog fluid. Secondly, the material can accurately mimic the mechanical properties of blood vessels, especially the vena cava. In testing venous vessels to determine a stress-strain relationship, Hamedani *et al.* calculated biaxial elastic moduli in the longitudinal and transverse directions. Vessel wall was characterized with elastic moduli ranging from 0.8 to 5.5 MPa[37]. Meanwhile, bulk mechanical testing of Sylgard 184 by Johnston *et al.* characterized the material with an elastic modulus ranging from 1.32 to 2.97 MPa[38], which falls cleanly into the expected range for the vessel walls of the inferior vena

cava. While the elastic modulus does not define the entire behavior of a material, it is useful here as a comparator confirming material similarity indicating that Sylgard 184 can likely serve as a mechanical substitute in analysis.

Section 4.2: Experimental Setup

The Sylgard IVC model was mounted in an optically clear acrylic box constructed to fit the model so that each inlet or outlet of the model coincided with the wall of the box and could lead to the exterior. These inlets and outlets were connected to a flow loop designed to physiologically simulate the local venous system. Most of this loop was adapted from previous work done by Evan Fox in the lab, and a basic schematic of the loop is recreated here in Figure 4-3[36]. The flow conditions associated with the mock circulatory loop are discussed in detail in Section 4.5.

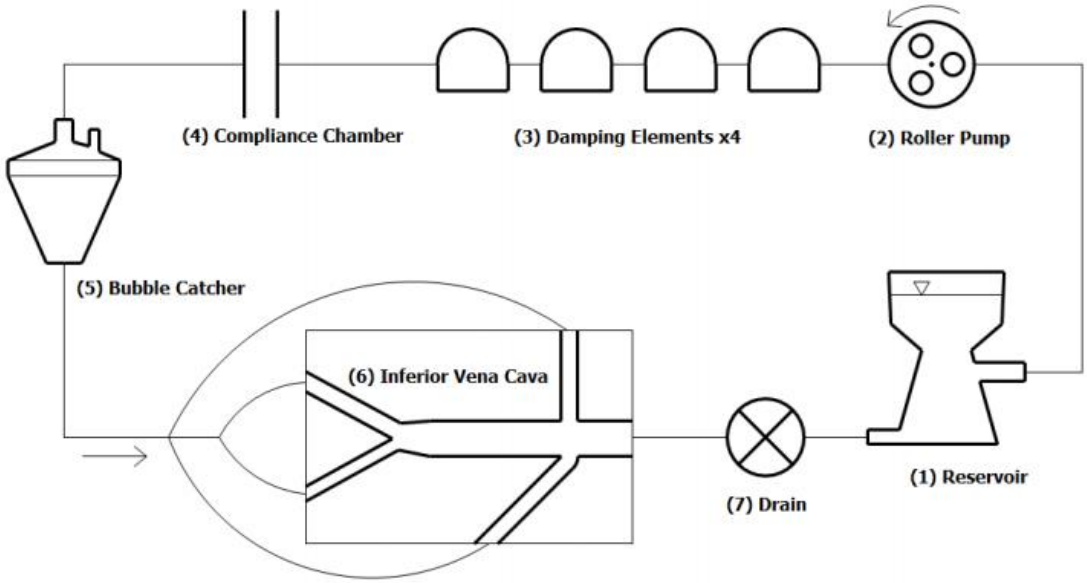

Figure 4-3. Venous circulatory flow loop[36]

While the flow loop used in the previous work is essentially unchanged to recreate similar physiological conditions, the acrylic chamber was altered to incorporate diaphragmatic compression on the IVC. Figure 4-4 shows a simplified schematic for the design of this chamber.

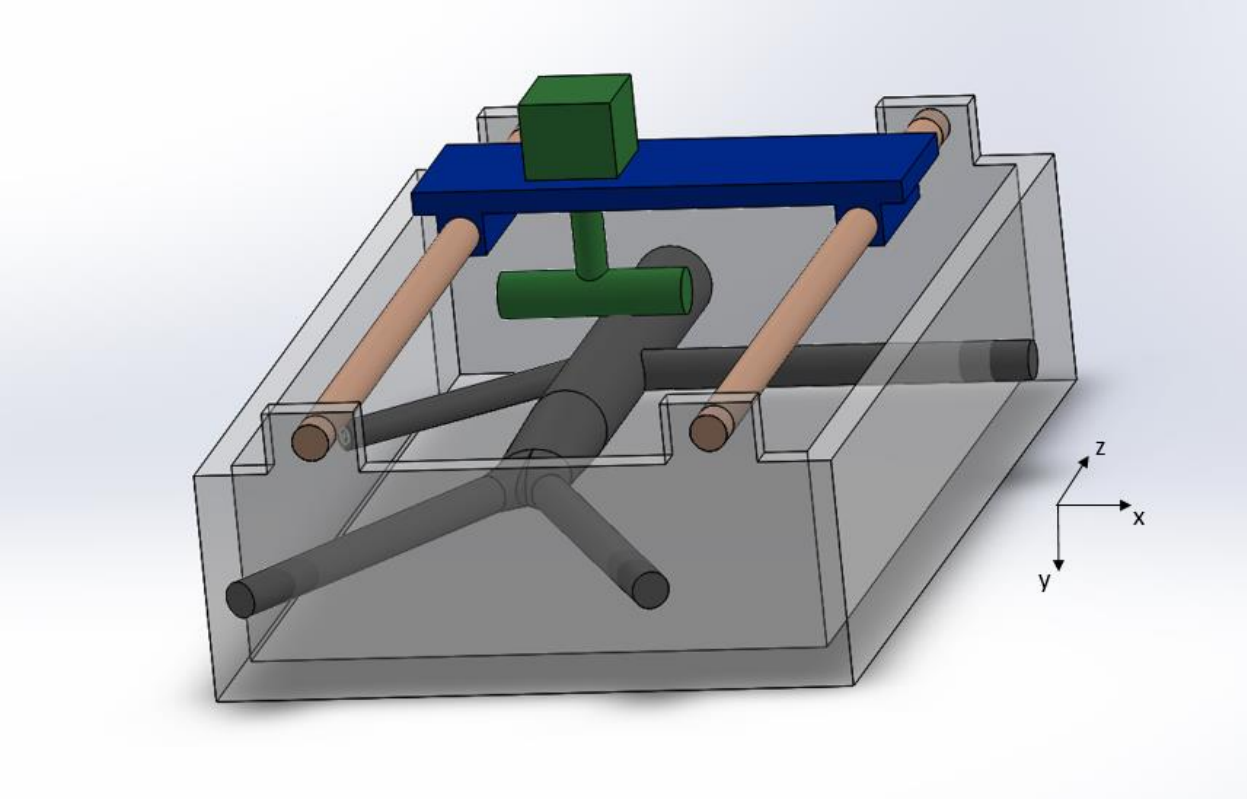

Figure 4-4. Simple SolidWorks render of acrylic chamber with mounted IVC model and roller system

In Figure 4-4, the Sylgard model was mounted in the acrylic chamber with slight tension, making sure that the bottom side of the model made contact with the base of the chamber, which imitated the support of the spine against the IVC. At the top of the box, a platform supported by two linear bearings was mounted on a rigid track. An external stepper motor (Adafruit Industries, New York, NY) controlled the z-direction motion of this platform, while a second motor mounted on the platform itself controlled the y-motion of a 0.5 inch diameter Delrin roller. The two motors were programmed independently to move the roller in the ±z and ±y –directions along the appropriate section of the IVC model in order to compress it in a manner analogous to diaphragmatic motion over the total limits of diaphragmatic

excursion observed in literature for varying amounts of respiratory effort. The exact quantities and implementation for this motion is discussed further in section 4.4.

When adjusted vertically in the y-direction, the roller can mimic any amount of compression on the IVC depending on the corresponding amount of respiratory effort. As was discussed earlier, the diaphragm was assumed, as a muscle, to be much more rigid than the low pressure, compliant vena cava. Therefore, the controlled variable here was not the load applied to the roller, but rather a specified positive y-displacement knowing that the roller can counter the resistive force of the IVC.

As observed in ultrasound imaging in Figure 3-5, the IVC deforms elliptically under compression from the diaphragm, with the minor diameter along the y-axis shortening and the major diameter along the x-axis elongating. In order to collect visual data on the deformation of the IVC, a camera was placed below the flow chamber to observe changes in the IVC's x-axis (major diameter) as the roller operates on the silicone model. Collecting this data assumes the IVC will deform elliptically such that two axes is sufficient to represent cross-sectional deformation.

Section 4.3: Blood Analog Fluid

In the flow loop, a Newtonian blood analog fluid was used, with a kinematic viscosity matching blood in order to recreate the fluid dynamics present in the body. The fluid was made of 45% volume glycerin in water as previously done in earlier lab work with IVC filters[36]. This provided a kinematic viscosity of 4.4 centiStokes (cSt). Because imaging was not required through the curved surface of the silicone model as in PIV, the refractive of Sylgard 184 was not matched with this fluid.

Section 4.4: Experimental Conditions

The goal of this experiment is to simulate the effect of diaphragmatic motion on the IVC over a varying range of conditions, from rest to exercise. Four conditions were tested with a focus on the diaphragmatic motion at rest, light exercise, heavy exercise, and during a Valsalva maneuver. All of these situations require varying flow conditions.

Cheng *et al.* studied the *in vivo* flow rates through the IVC in normal subjects and found that the mean flow rate through the vessel increased from 2.0 ± 0.5 L/min to 6.5 ± 1.4 L/min from rest to exercise[39]. As a result, when simulating more strenuous exercise, the flow rate in the loop must be adjusted accordingly. In this study, these two values were used for rest and exercise, with a third moderate value chosen to represent light exercise. Regardless of respiratory effects, the flow in the IVC is best modeled as steady flow, so a steady flow pump was used, ignoring heart rate changes due to exercise. In all conditions, flow from the renal veins was consistently restricted to 0.6-0.8 L/min to reflect an increased metabolic demand increasing blood flow from the lower extremities only.

Roller motion waveforms were determined from several physiological variables. The amplitude of these waveforms can best be expressed by the total movement of the diaphragm during a respiratory cycle, or the total diaphragmatic excursion (TDE). O. L. Wade found in an early study that the average TDE in an erect subject was around 16 mm in quiet breathing (resting) and 92 mm in deep breathing (heavy exercise)[40]. The frequency of respiratory rate can then be used as a frequency of diaphragmatic motion and varies from about 12 to 20 breaths/ minute in a normal subject[41], and the waveform shape presented in Figure 3-6 most closely matches a triangle wave. Intermediate values were again chosen to simulate the light exercise condition. Coupled with the values for amplitude and frequency, a triangular waveform was programmed into the motor controlling the motion of the roller.

Lastly, the collapsibility index is an important characteristic of any of these states. While the index can take any value from 0 to 100%[33], typical ranges can be defined for exercise states. These can

be loosely defined as 0-30% for resting, 30-50% for light exercise, and 50-100% for heavy exercise. Midpoints of these ranges were used to simulate each state.

As a sudden forced attempted exhalation, the Valsalva maneuver was simulated using the flow rate that accompanies a resting physiological state. From literature, the cIVC value associated with the maneuver ranged 30.9 ± 4.8% in a study of ten patients, so a value of 30% was chosen for simulation. Since this maneuver is not cyclic in nature, but rather performed once, breathing frequency and TD, which correspond to amplitudes and frequencies of roller movement waveforms are irrelevant parameters for this condition. For clarity, all experimental conditions used are summarized in Table 4-2.

Table 4-2. Flow Loop and Diaphragmatic Motion Values for Exercise Conditions

Condition	**Flow Rate (L/min)**	**cIVC**	**Frequency (min^{-1})**	**TDE (mm)**
Resting	2.0	15%	12	16
Light Exercise	4.3	40%	16	54
Exercise	6.5	75%	20	92
Valsalva	2.0	30%	-	-

Videos were recorded for the roller motion and resulting compression for a total of five trials under each condition. Still frames were isolated from these videos at specific points for analysis of the IVC compression. From each video taken, five still frames were isolated when the roller was positioned at -50%, -25%, 0%, 25%, and 50% of its full range of motion, based on the midpoint of the motion. Figure 4-5 gives a better representation of these locations, drawn on the light exercise condition. For each of the frames below, the roller was used as a scale bar to measure the length of the long axis as the vessel expands horizontally

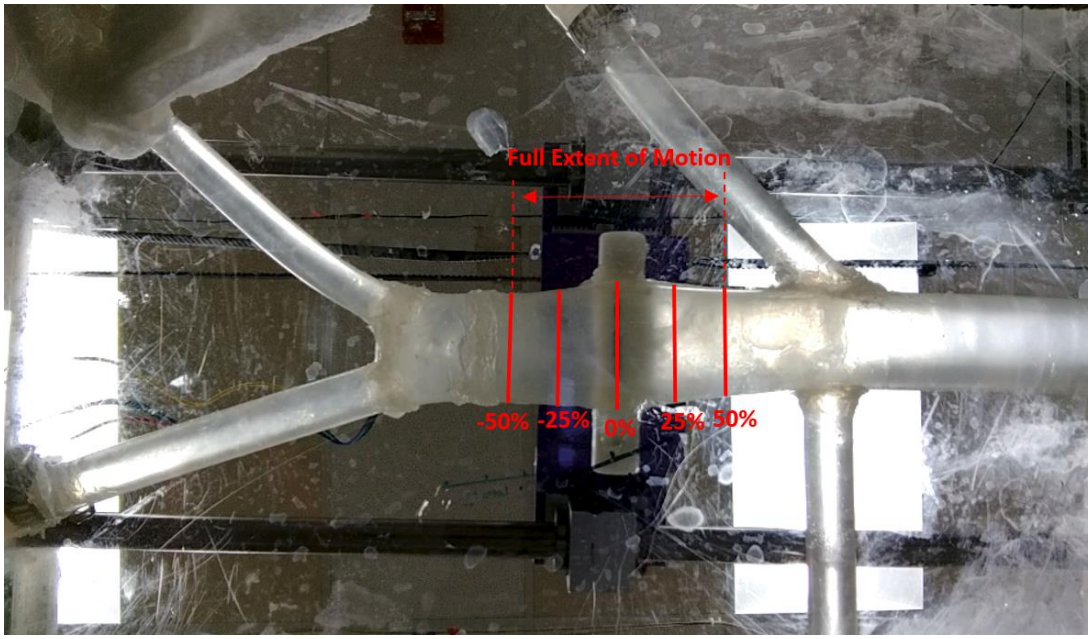

Figure 4-5. Sample roller positions for measuring long axis deformation during IVC compression

Section 4.5: Flow Conditions

To measure flow rates through the inlets and outlets of the IVC model, a Transonic TS410 transit-time tubing flowmeter was used, along with one ME 8XL flow probe and one ME 20XL flow probe (Transonic Systems, Ithaca, NY). The 8XL probe was used on the smaller inlet tubing representing the iliac and renal veins, while the 20XL probe was used to measure the total flow through the outlet. Before any data were collected, these probes were calibrated with known flow rates through a straight tube. The output voltage from each probe was measured at zero flow and five appropriate flow rates spanning the entire range expected in this model. Flow rate in L/min and output voltage in V were plotted, and a linear regression performed to find a calibration curve. Figure 4-5 and 4-6 show the calibration plots, including regression equations and R-squared values, for the 20XL and 8XL probes, respectively.

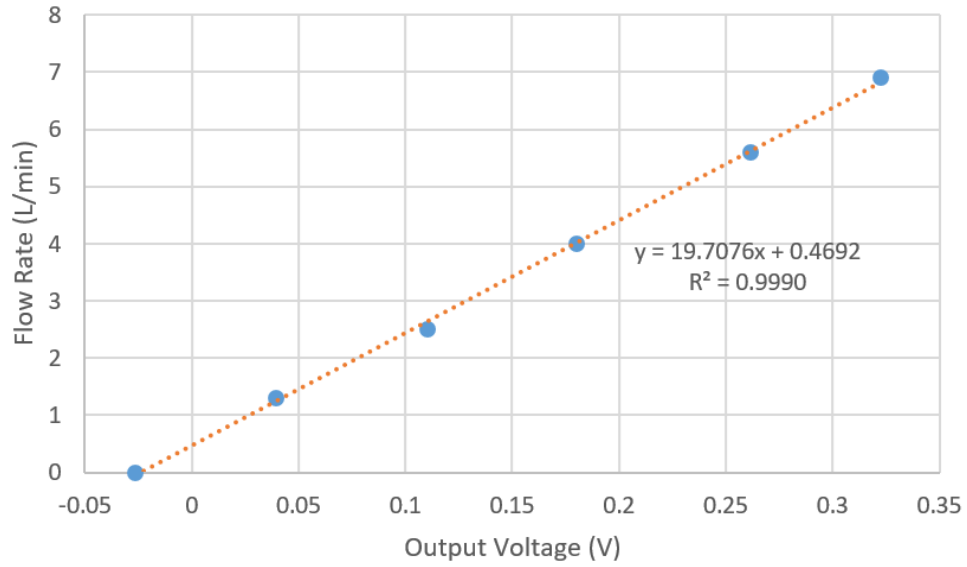

Figure 4-6. Flow probe calibration for 20XL probe measuring total outlet flow

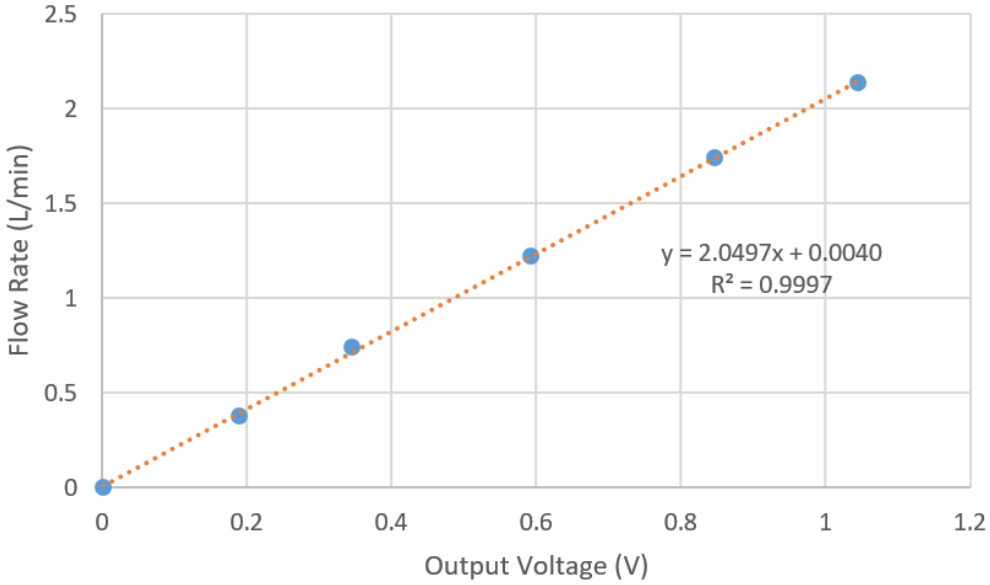

Figure 4-7. Flow probe calibration for 8XL probe measuring individual inlet flows

During data collection, the flow conditions through the IVC model were monitored for both flow rates and pressure. The flow rates through all inlets were measured once at the beginning of data collection, while the total flow rate through the outlet and the inlet flow rate through the left iliac vein were measured continuously with the two flow probes. Even though only a net flow rate was specified in

section 4.4, the flow rate through all of the inlets was adjusted for each condition so as to limit the renal inlets to 0.6 – 0.8 L/min. This reflects the fact that higher exercise loads do not significantly affect blood flow through the kidneys and more strongly affects the venous return from the lower extremities. Additionally, pressure was measured via a pressure tap just past the outlet of the silicone IVC model.

Flow rates through the outlet and left iliac inlet, and vessel pressure were measured continuously throughout data collection. Due to signal noise, this data was filtered in MATLAB (Mathworks, Natick, MA) using an 80^{th} order low pass filter with a frequency cutoff of 10 Hz (significantly higher than any stimulation provided to the system). Waveforms were not collected during a Valsalva maneuver due to its stationary nature.

Chapter 5

Computational Simulation Materials and Methods

Section 5.1: COMSOL Simulation

In order to provide a basic validation of the experimental platform, the Solid Mechanics module of COMSOL Multiphysics (COMSOL, Burlington, MA) was used to create a computational simulation of a section of vena cava at the location studied in the experimental platform. This simulation was performed after gathering data from the experimental platform, then solved under identical environmental conditions, using the vena cava properties and vessel wall geometry. The results were analyzed for the same deformation values in the major axis expansion of the cross section as were the experimental data for comparison.

Section 5.2: Simulation Geometry and Materials

For the simulation, a 100 mm straight section of the IVC between the iliac and renal veins was modeled, which is analogous to the region of the experimental silicone model that experiences deformation during roller motion. The lumen of the simulation model was identical in initial shape to the Sylgard 184 model used in the experimental platform. This elliptical cross-section was 26 mm along the short axis and 28 mm along the long axis. As a simulation of the vena cava, the vessel wall was made to 1.5 mm thick[42]. A 1.0 mm thick case was also simulated to match the experimental silicone model. A flat plate was modeled underneath the vessel to mimic the support of the bottom of the acrylic chamber. Lastly, a roller of the same diameter as used in the experimental platform was modeled above the vessel at the point of zero compression. Altogether, only half of the model was drawn in COMSOL to take advantage of a plane of symmetry. Figure 5-1 displays a cross-section of the half-symmetry in the middle of the model and a full 3D version of the entire model.

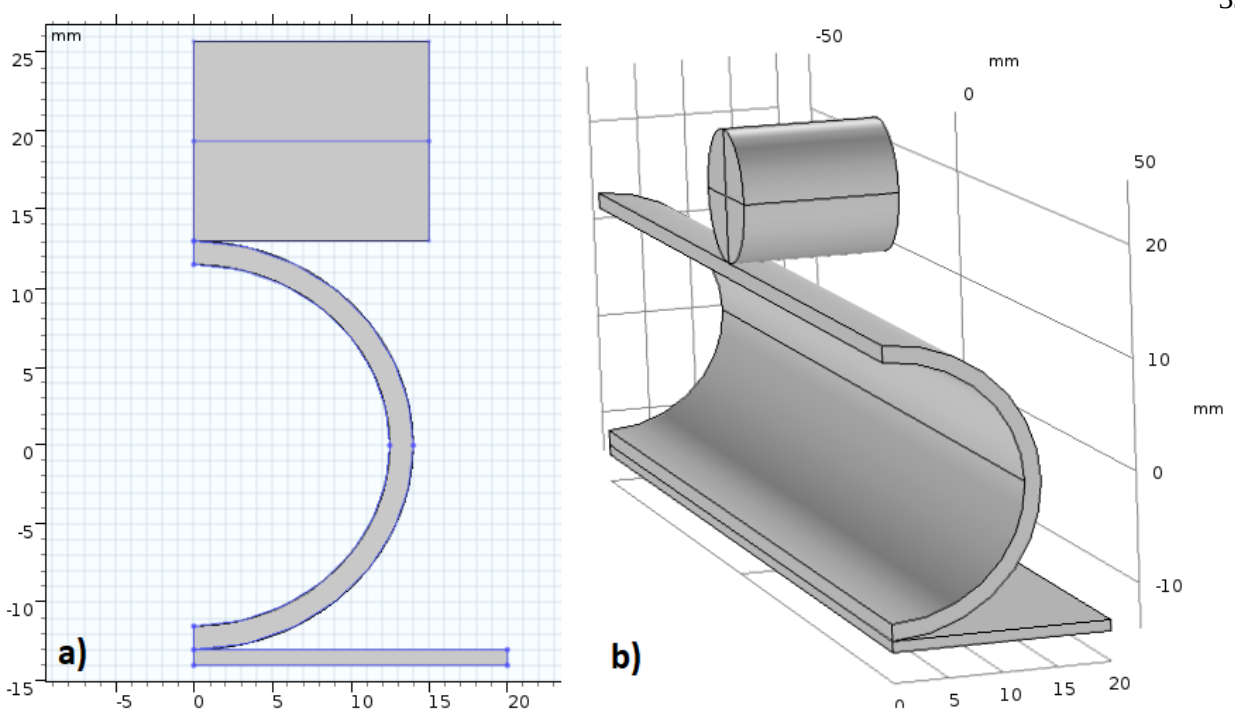

Figure 5-1. COMSOL simulation geometry showing a) midplane cross-section and b) full 3D geometry for 1.5 mm thickness

Several material choices were made to allow COMSOL's Solid Mechanics to produce a computational solution. For a linear elastic material, the elastic modulus, density, and Poisson's ratio had to be specified. The vessel itself was modeled using typical properties of vena cava[37]. The bottom plate and roller were modeled as acrylic and Delrin, respectively, using COMSOL's materials library. Table 5-1 gives a summary of the mechanical properties of each material. As displayed in the table, the vessel wall has a much less rigid elastic modulus by three orders of magnitude, so this simulation essentially treats the roller and base as rigid surfaces.

Table 5-1. Mechanical properties of IVC, base of chamber, and roller used in simulation

Material	**Elastic Modulus (MPa)**	**Density (kg/m^3)**	**Poisson's Ratio**
Vena Cava	3.15	1030	0.40
Acrylic	3200	1190	0.35
Delrin	2410	1420	0.35

Section 5.3: Simulation Mesh and Boundary Conditions

The mesh used for this simulation was generated automatically by COMSOL based on the choice of physics being simulated. The specific option chosen was "extra fine", which generated a mesh of tetrahedral elements with edge sizes on the order of 0.5 mm. Once this mesh was chosen, various boundary conditions were set to mimic physiological conditions. Figure 5-2 gives a visual overview of the boundary conditions put in place for this simulation.

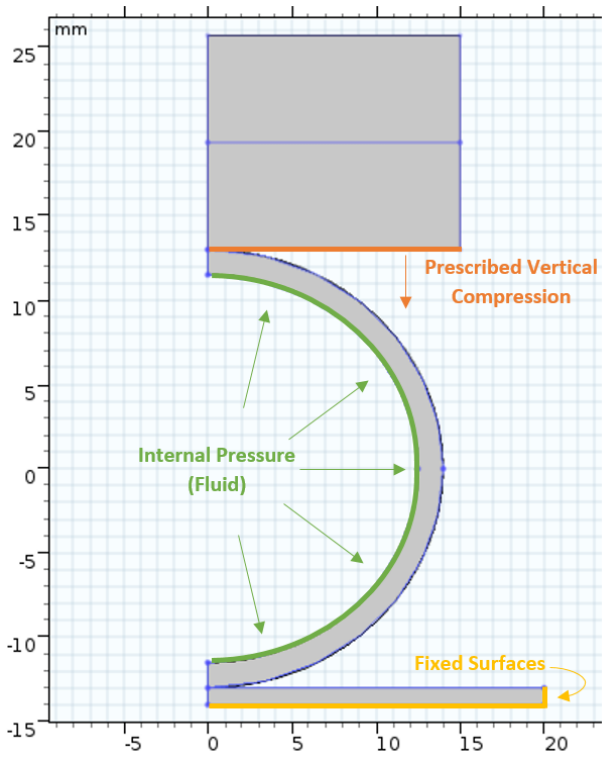

Figure 5-2. Midplane cross-sectional geometry showing surfaces and applied boundary conditions

First and foremost among these conditions, the flow itself was not simulated, but rather the pressure it exerts on the vessel walls was simulated as an applied load perpendicular to the wall at all points. Next, the bottom and sides of the base plate as well as the ends of the vessel section were treated as fixed points, akin to the acrylic chamber experimentally. Lastly, the roller was given a prescribed displacement in the y-direction corresponding to the physiological condition being simulated (rest, light

exercise, heavy exercise). In the cases of internal pressure and vertical displacement, values were set equal to those found experimentally in section 6.2 for similarity.

Section 5.4: Roller Simulations

One of the first uses of this simulation was to select a correct size for the roller, with it being the main component performing all compression. At three different levels of vertical compression spanning a large range of IVC collapsibility index, four roller sizes ranging from 2.5 mm to 15 mm in radius were simulated. As in all results in this study, the deformation of the major axis as the IVC expands was measured. Figure 5-3 shows that this expansion did not vary as a function of roller radius, indicating that similar compression could be achieved with any roller size. From this, a 12.7 mm radius roller (1/2" diameter) was chosen because of material availability.

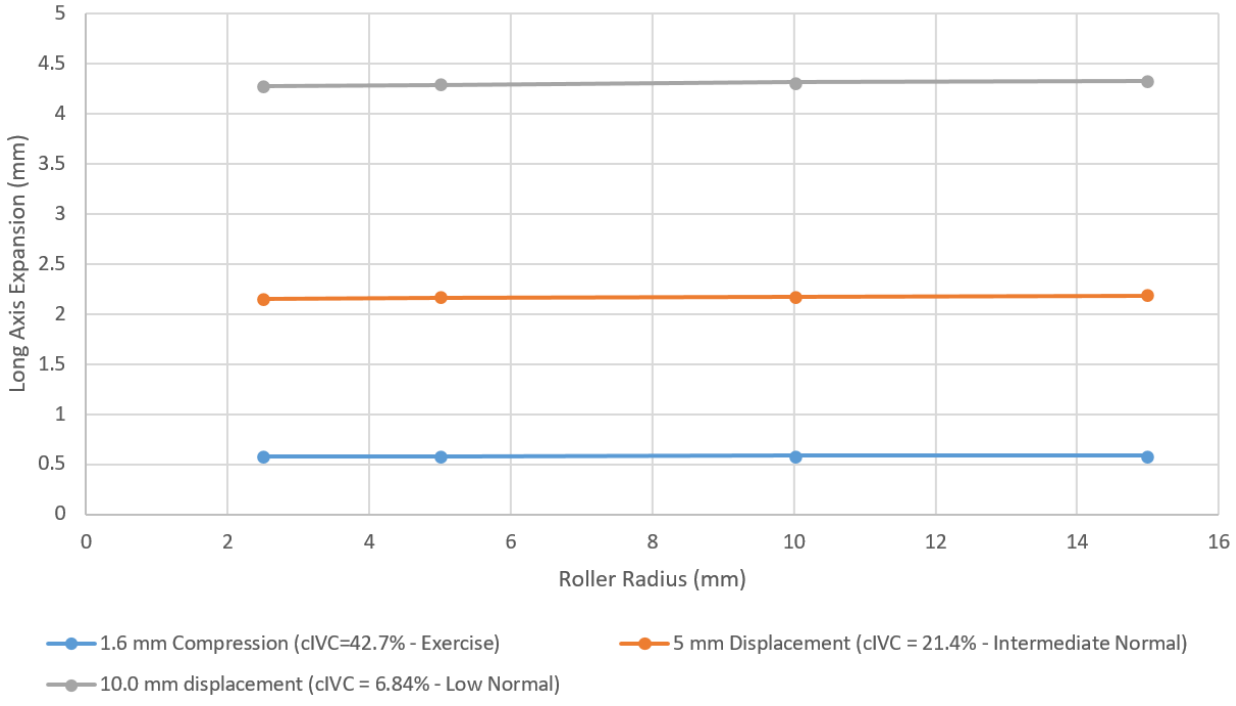

Figure 5-3. IVC cross-section deformation along the horizontal x-axis as a function of roller radius shows no dependency between variables

Chapter 6

Results

Section 6.1: Flow Conditions

Table 6-1 presents the steady flow variables characterizing each flow condition before any dynamic compression of the IVC. In this table, the total outlet flow rates are reported along with the individual inlet flow rates and the pressure directly past the silicone model's outlet. Average values between all five data sets are reported with standard deviations. Valsalva maneuver and resting conditions were tested under the same flow conditions.

Table 6-1. Measured flow rates for all inlet and outlets during each physiological condition

(L/min)	**Rest**	**Light Exercise**	**Heavy Exercise**	**Valsalva**
Outlet (Total)	2.40 ± 0.05	4.23 ± 0.04	6.23 ± 0.05	2.40 ± 0.05
Left Renal	0.60 ± 0.06	0.74 ± 0.03	0.69 ± 0.03	0.60 ± 0.06
Right Renal	0.61 ± 0.05	0.76 ± 0.05	0.70 ± 0.02	0.61 ± 0.05
Left Iliac	0.58 ± 0.07	1.29 ± 0.07	2.43 ± 0.04	0.58 ± 0.07
Right Iliac	0.61 ± 0.05	1.44 ± 0.08	2.41 ± 0.07	0.61 ± 0.05
Pressure (mm Hg)	6.67 ± 0.12	6.36 ± 0.06	6.23 ± 0.09	6.67 ± 0.12

Figure 6-1 plots the waveforms recorded during roller movement under the resting condition, including the total outlet flow rate, inlet flow rate through the left iliac vein, and vessel pressure. The roller motion profile is also included for reference. During this condition, all three flow variables continuously measured remained steady with time.

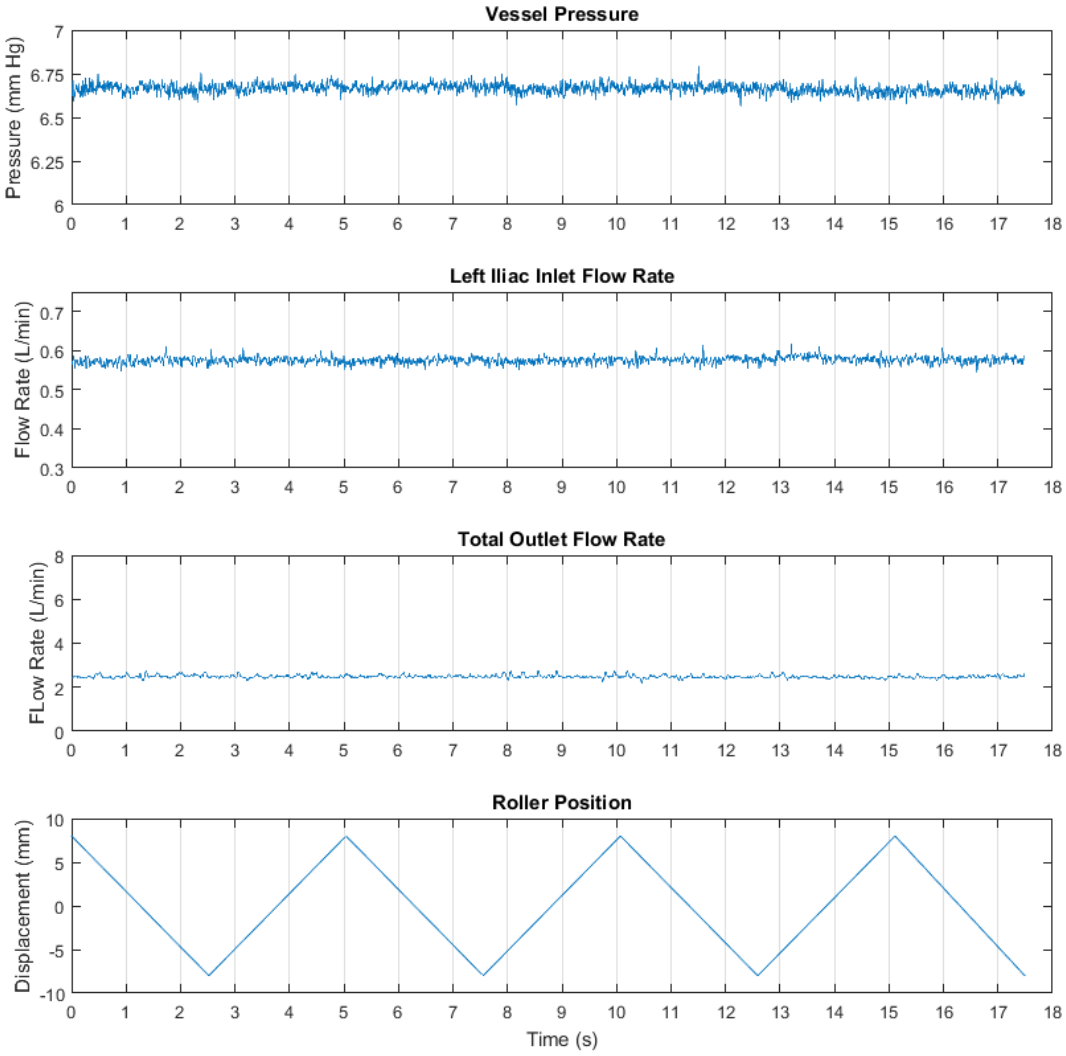

Figure 6-1. Dynamic flow conditions during resting experimental condition (16 mm TDE at 12 breaths/min), including (from top) vessel pressure, left iliac inlet flow rate, total outlet flow rate, and roller position with time

Figure 6-2 presents analogous waveforms to those presented in the previous figure, but for the light exercise condition. Again, both flow rates through the silicone model and the vessel pressure are approximately steady. Between the resting and light exercise condition flow results there is a change of scale to reflect increased flow rates as well as a larger range of roller motion as total diaphragmatic excursion increases.

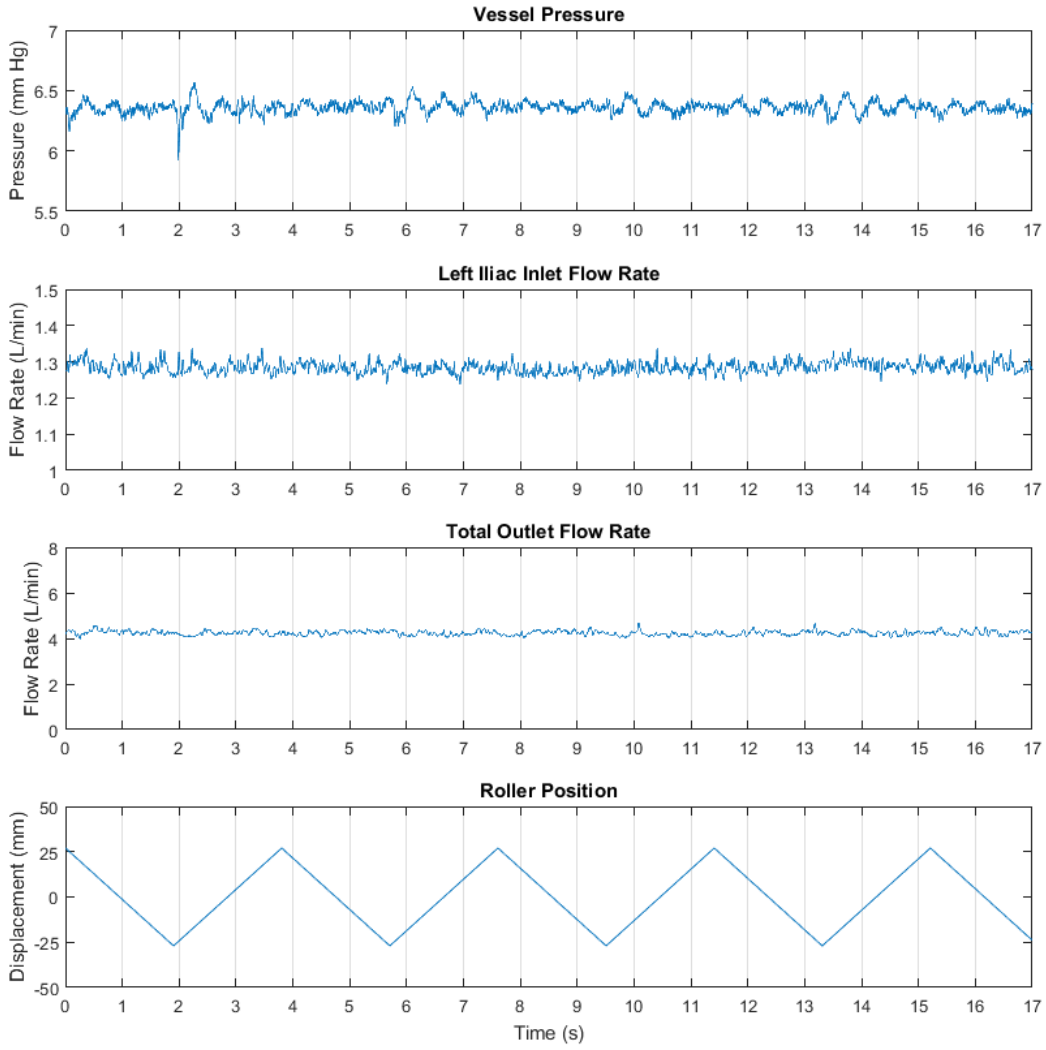

Figure 6-2. Dynamic flow conditions during light exercise experimental condition (54 mm TDE at 16 breaths/min), including (from top) vessel pressure, left iliac inlet flow rate, total outlet flow rate, and roller position with time

Lastly, Figure 6-3 depicts the vessel flow rates and pressure for the heavy exercise condition. As opposed to the other two conditions, a degree of pulsatility is clearly observed in these waveforms and is both periodic and in unison with the roller motion profile. Again, the change of scales is important to note with increasing variable magnitudes.

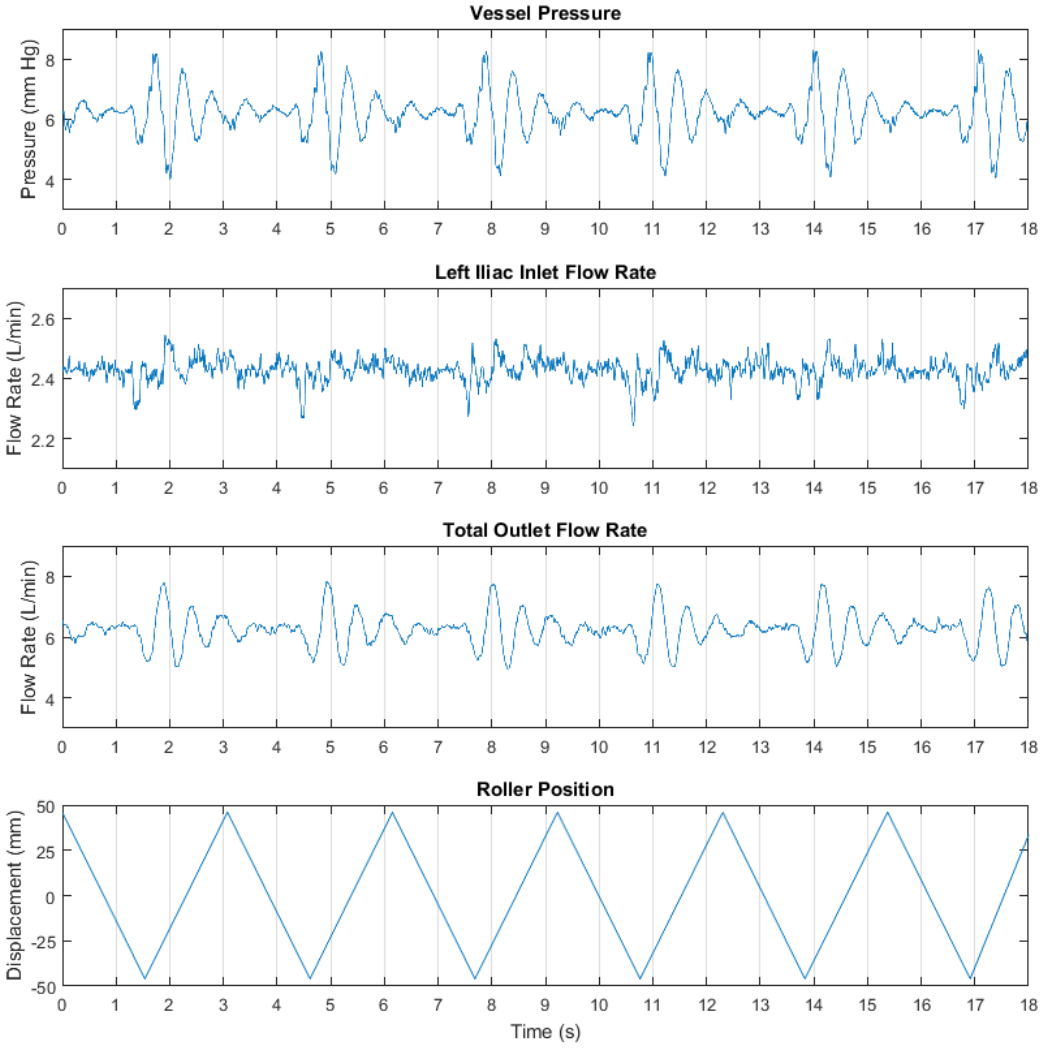

Figure 6-3. Dynamic flow conditions during heavy exercise experimental condition (92 mm TDE at 20 breaths/min), including (from top) vessel pressure, left iliac inlet flow rate, total outlet flow rate, and roller position with time

Section 6.2: Experimental Results

Figure 6-4 contains sample frames taken at the 0% midpoint of roller motion for all four experimental cases. In the figure, the dashed lines and arrows highlight the elongation of the major axis as the IVC model is compressed. Clearly, an increase in the severity of compression (higher cIVC) results in larger deformations along the major axis of the model. While the Valsalva maneuver sample is

listed last as Figure 6-4d, its cIVC ratio actually falls between that of the resting and light exercise samples in Figures 6-4a and 6-4b.

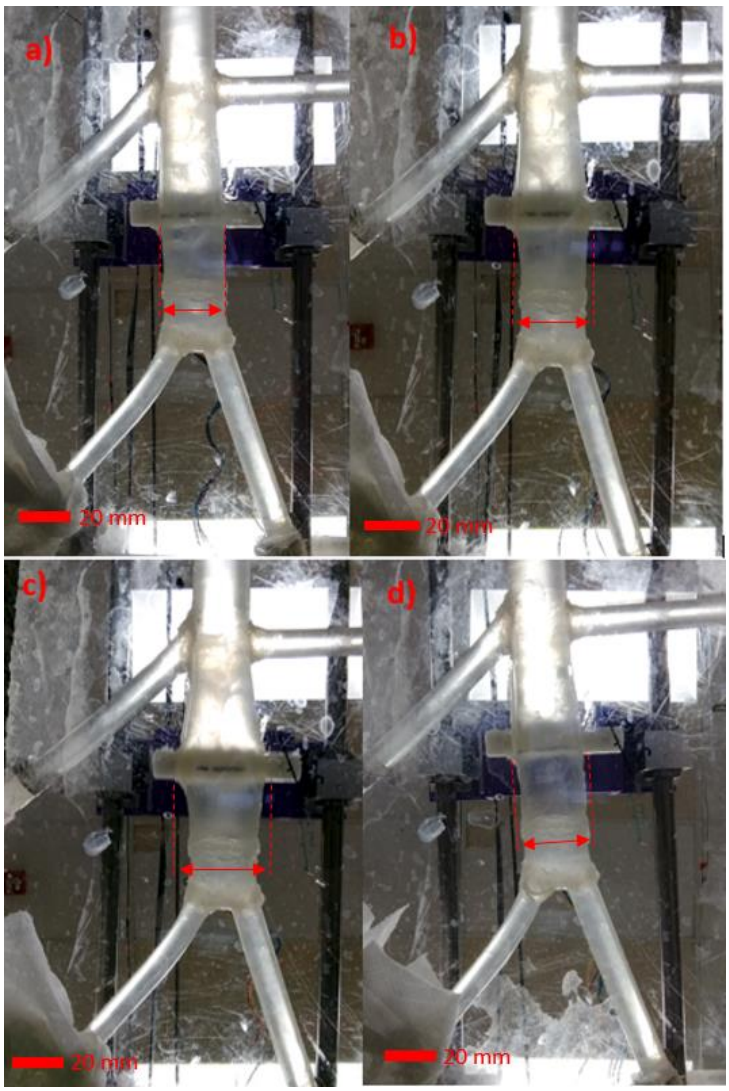

Figure 6-4. Minor axis compressions and resulting major axis expansions viewed from below the model chamber for a) rest, b) light exercise, c) heavy exercise, and d) Valsalva maneuver

Before analyzing the horizontal deformations associated with compression, the vertical compression itself was analyzed to ensure it was close to the target values of cIVC presented in section 4.4. Table 6-2 presents the cIVC values for each experimental condition.

Table 6-2. Experimentally actualized vertical compression values for each condition

	Rest	Light Exercise	Heavy Exercise	Valsalva
Target cIVC	15%	40%	75%	30%
Experimental Compression (mm)	4.2	11.1	19.7	8.2
Experimental cIVC	16.1%	42.6%	75.8%	31.6%

The resulting deformations of the major axis under compression are then reported in Table 6-3. In this table, the average value at each roller position was reported for all four experimental conditions along with the overall average value for individual conditions. However, standard deviations were only calculated for the overall average values so as to represent the entirety of all five data sets for each experimental condition. Additionally, the mean values were normalized by the initial axis length to calculate an axis strain. A positive trend can be observed in the strain values with increasing cIVC values.

Table 6-3. Experimental major Axis (x-axis) deformation under compression for each test condition

(mm)	**Rest**	**Light Exercise**	**Heavy Exercise**	**Valsalva**
-50%	1.60	2.49	7.69	-
-25%	2.55	2.03	8.12	-
0%	1.67	4.33	7.506	-
+25%	1.73	3.67	7.99	-
+50%	2.01	4.52	7.83	-
Mean	1.91 ± 0.44	3.41 ± 0.55	7.83 ± 0.64	2.35 ± 0.31
Normalized	0.0682 ± 0.0157	0.122 ± 0.020	0.280 ± 0.023	0.0839 ± 0.0111

Section 6.3: Computational Results

Figure 6-5 plots visual simulation results for the vena cava model with physiological 1.5 mm wall thickness for all conditions. Figure 6-6 presents analogous results for the same model with the experimental silicone model's 1.0 mm wall thickness. Simulation data were used to create both a 3D and 2D perspective for each condition. For both perspectives, a wireframe representation of the roller and vena cava before any compression is included for reference.

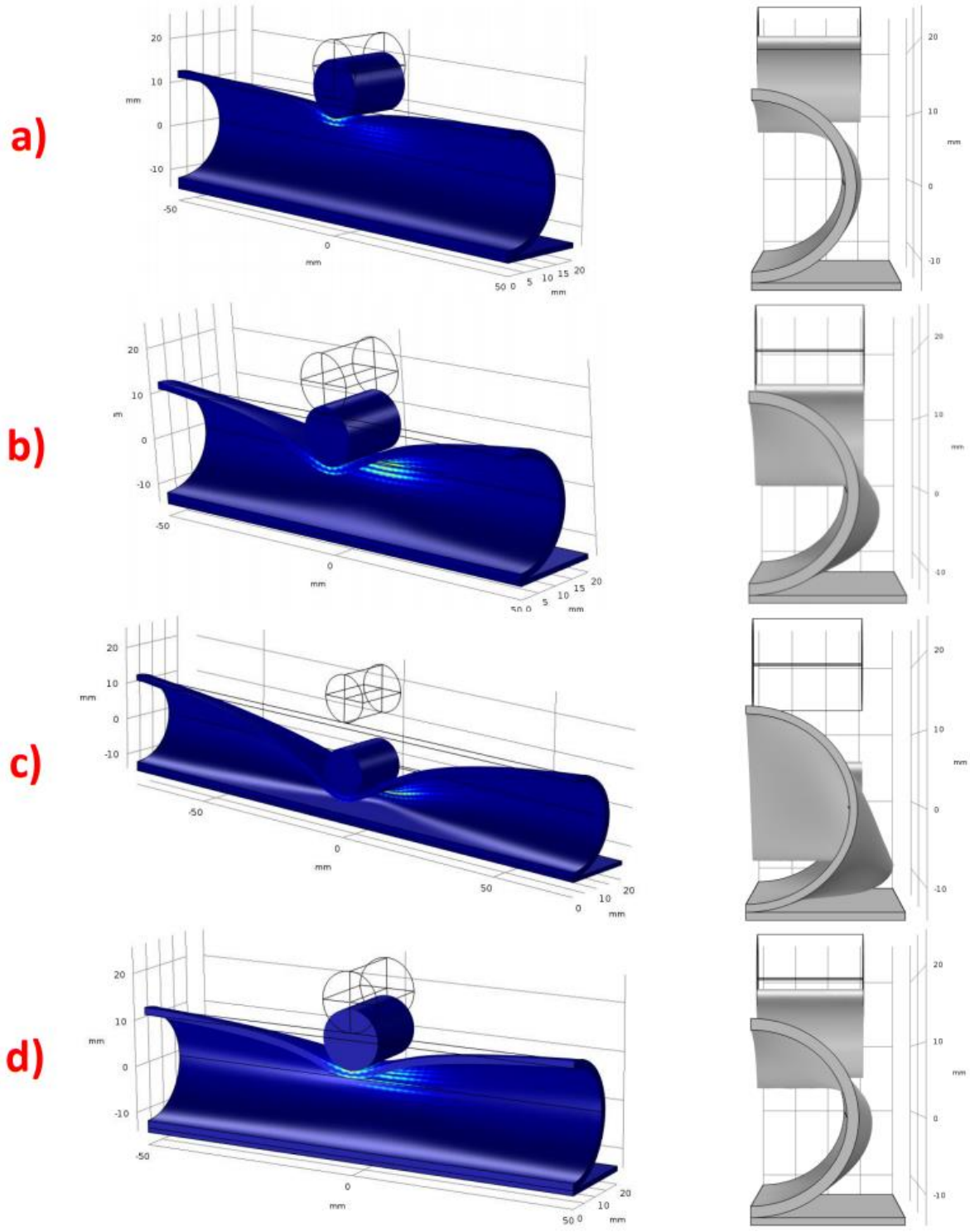

Figure 6-5. 3D and 2D geometric plots of the 1.5 mm thick model for the a) resting, b) light exercise, c) heavy exercise, and d) Valsalva maneuver conditions

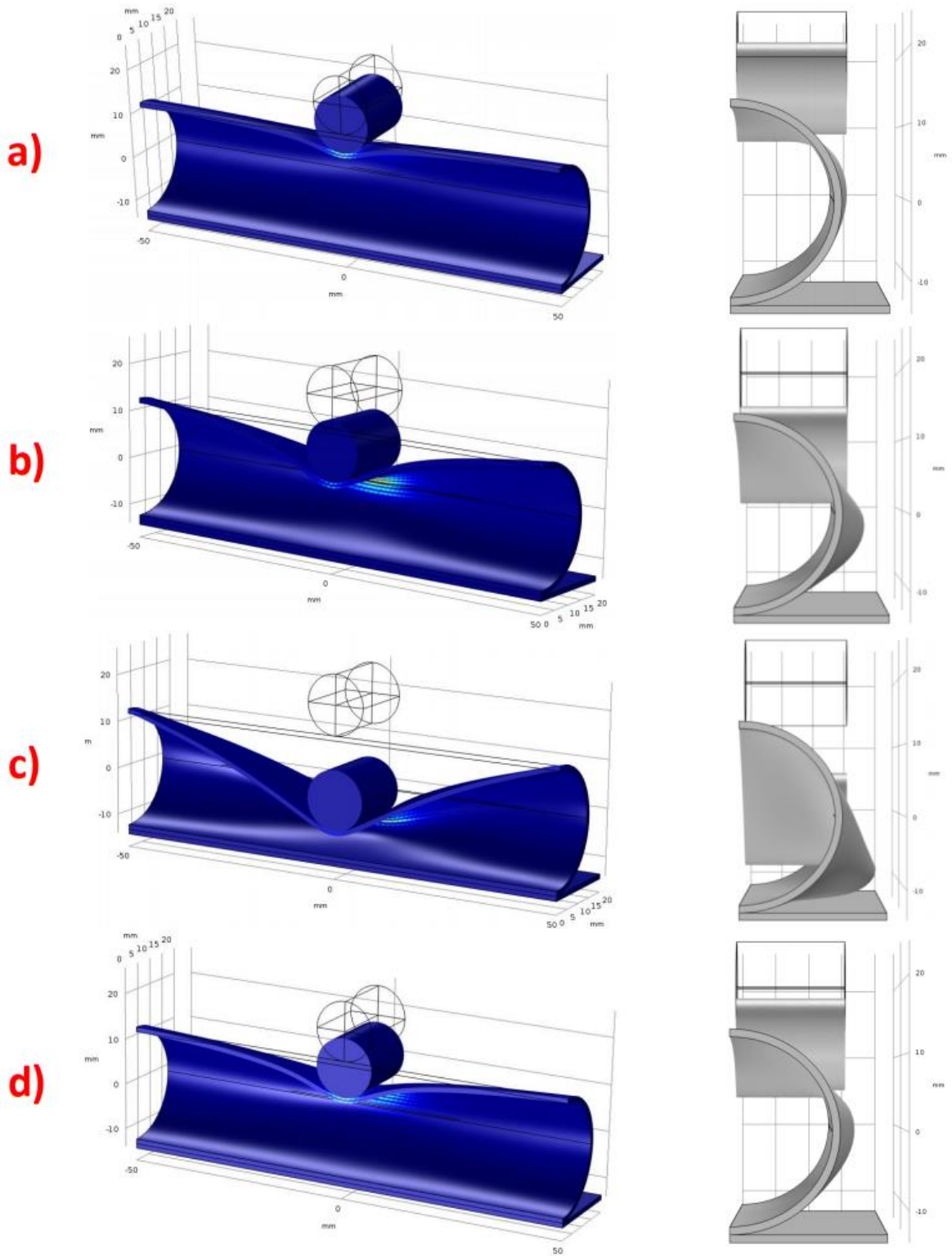

Figure 6-6. 3D and 2D geometric plots of the 1.0 mm thick model for the a) resting, b) light exercise, c) heavy exercise, and d) Valsalva maneuver conditions

Exact numerical quantities are reported in Table 6-4 for the major axis extension in both the 1.5 mm thick and 1.0 mm thick models. Again, these deformations were normalized by the initial length of the axis to calculate a major axis strain quantity.

Table 6-4. Computational major axis (x-axis) deformation under compression for each test condition

Model		**Rest**	**Light Exercise**	**Heavy Exercise**	**Valsalva**
	cIVC	16.1%	42.6%	75.8%	31.6%
1.5 mm	***Major Axis Deformation (mm)***	1.65	3.17	5.15	2.24
	Major Axis Strain (mm/mm)	0.0589	0.113	0.184	0.0800
1.0 mm	***Major Axis Deformation (mm)***	1.67	3.32	5.30	2.29
	Major Axis Strain (mm/mm)	0.0596	0.119	0.189	0.0818

Chapter 7

Discussion

Section 7.1: Comparison of Experimental and Computational Results

The ultimate goal of this project is to create an experimental platform that is capable of simulating the IVC's *in vivo* collapse for a range of physiological conditions so that further studies of IVC filter performance and hemodynamics can incorporate this dynamic motion. To satisfy this requirement, the proposed experimental platform should be able to quantitatively match the geometric deformations measured in the vena cava under specific degrees of collapse. This concept demonstrates the necessity of comparing the experimental results presented in Section 6.2 to the computational studies performed using vena cava properties in order to validate the platform.

Even though the need for a computational study arises from the unavailability of specific quantitative data in literature during a wide range of conditions, a brief comparison to literature can be performed qualitatively in each condition and quantitatively for the Valsalva maneuver condition. For a qualitative analysis, Figure 7-1 shows a reconstructed IVC with local compression in the infrarenal region during moderate breathing.

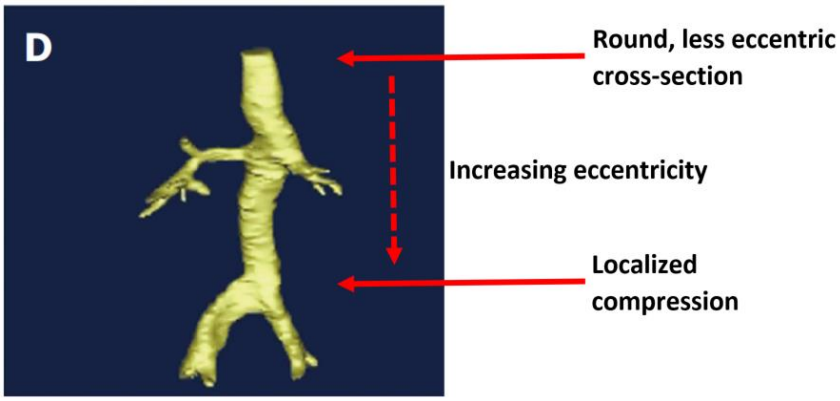

Figure 7-1. Locally compressed IVC during breathing reconstructed from CT data (adapted from Laborda et al., 2014)[43]

Following the arrows in the figure from top to bottom, there is a gradual transition from a rounder elliptical cross-section above the renal veins to a highly eccentric elliptical cross-section at the localized compression in the lowest portion of the infrarenal IVC. Figure 6-4 presents a similar shape produced by the experimental platform under each test condition. Luckily, data are readily available for IVC collapse during Valsalva maneuvers. Murphy *et al*. performed a study of cross-sectional deformities in the IVC during Valsalva maneuvers and reported an initial major axis value of 23.2 mm varying by an average 1.0 mm in either direction[31]. When a major axis strain is calculated, Murphy *et al*. found a 0.0862 mm/mm strain, in good agreement with the 0.0818 mm/mm observed experimentally in this work.

Table 7-1 provides an initial comparison of the experimental and computational data sets from Chapter 6, summarizing the major axis deformations in mm at the cIVC tested at the resting, light exercise, heavy exercise, and Valsalva maneuver conditions. Within all cases, both experimental and computational, the change in major axis length increased nearly linearly with cIVC. This trend was expected, as the major axis should expand further under more severe minor axis compression. While these positive trends within each model are significant, the trends observed *between* models are more notable. At any one cIVC value, the three models have consistent relative magnitudes, with the experimental model experiencing the highest strain, followed by the 1.5 mm thick computational model with the lowest strain.

Table 7-1. Comparison between experimental and computational major axis (x-axis) deformation under compression for each test condition

	Rest	**Light Exercise**	**Heavy Exercise**	**Valsalva**
Target cIVC	15%	40%	75%	30%
Experimental cIVC	16.1%	42.6%	75.8%	31.6%
Exp. Major Axis Deformation (mm)	1.91 ± 0.44	3.41 ± 0.55	7.83 ± 0.64	2.35 ± 0.31
Comp. Major Axis Deformation, 1.5 mm (mm)	1.65	3.17	5.15	2.24
Comp. Major Axis Deformation, 1.0 mm (mm)	1.67	3.32	5.30	2.29

For a comprehensive visual comparison, Figure 7-2 plots all three datasets. The top chart of this figure plots the major axis strain for each experimental and computational data set against cIVC. A percent difference between experimental data and each of the two simulations (1.5 mm and 1.0 mm wall thickness) was calculated and plotted in the bottom chart of Figure 7-2. In the top plot, approximately the same linear increase in strain with cIVC is evident in the data with the exception of a deviation in the experimental data set at the highest cIVC value. Again, important trends appear *between* plots for all cIVC values. As noted before, each model consistently outputs strain values with magnitudes in the same relative order without any overlap. Specifically, the experimental platform always produces the largest strains, followed by the 1.0 mm thick simulation then the 1.5 mm thick simulation. In fact, the bottom chart of percent differences serves to highlight the consistently greater percent difference between the experimental and the 1.5 mm thick computational data set than between the experimental and 1.0 mm thick computational data set.

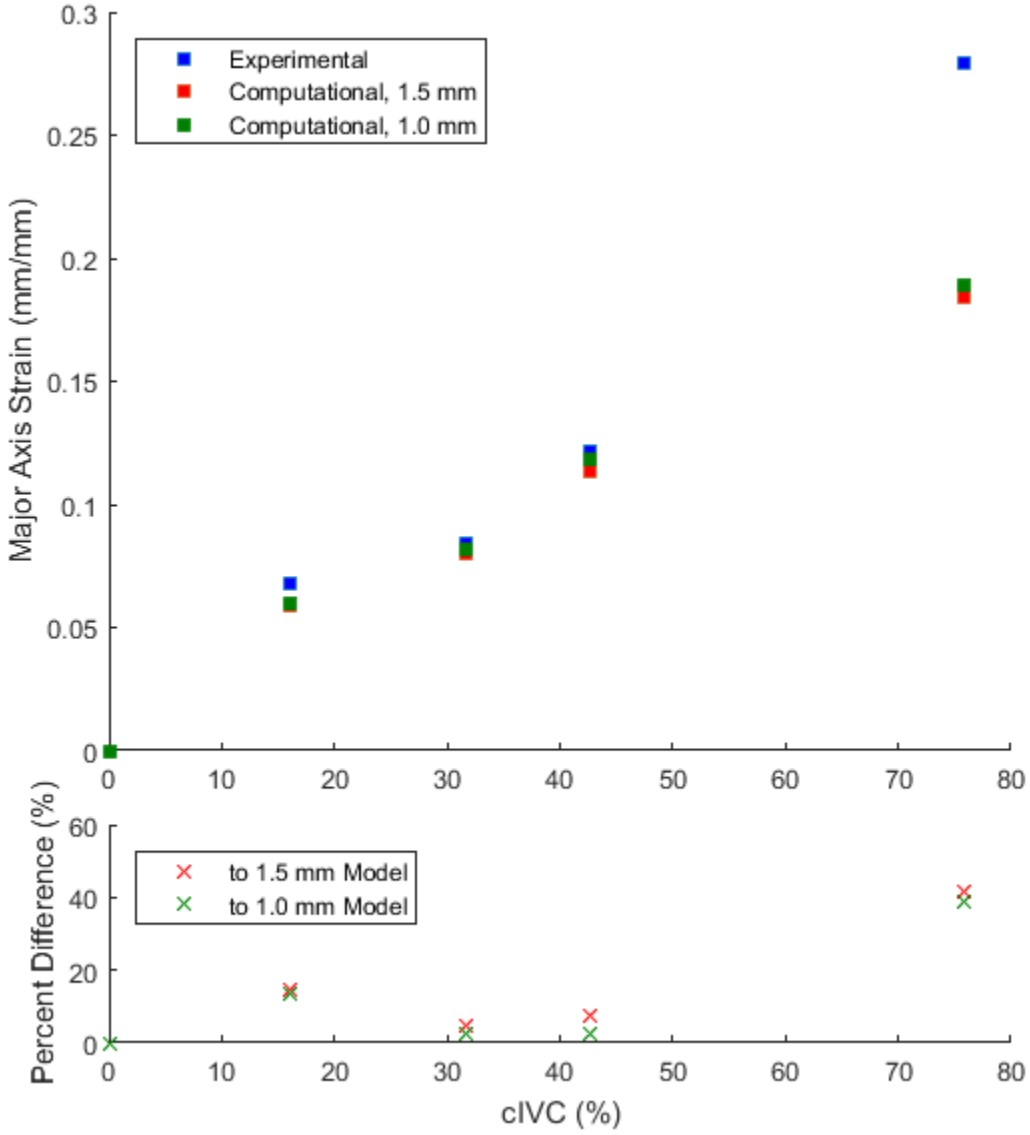

Figure 7-2. Experimental, computational (1.5 mm wall thickness), and computational (1.0 mm wall thickness) major axis strain (top) and percent differences between experimental and computational studies (bottom) against cIVC

This particular trend suggests a sort of convergence from the experimental platform towards the thicker simulation model. While both cases were simulated with vena cava mechanical properties, the 1.5 mm thick case is the one that is actually more physiologically relevant to an *in vivo* vena cava and is therefore more desirable for the experimental platform to accurately replicate in terms of cross-sectional deformations. The 1.0 mm thick case serves more as an intermediate, exploring material thickness effects

through its ability to match the exact wall geometry of the silicone model used experimentally. Intuitively, it would be expected that, given similar properties to vena cava tissue, a silicone model would more closely replicate a simulation with identical geometry rather than one slightly thicker. This consistent "stacking" of plots over the entire tested cIVC domain supports this intuition, strongly implying that a 1.0 mm thick Sylgard 184 model can imitate 1.0 mm thick vena cava tissue and will only shift closer and closer to imitating physiological vena cava tissue as its thickness approaches that of the 1.5 mm thick computational model.

Further explanation and interpretation of the relationship between data sets lies in the expected compliance of each model. Thin-walled structures will have higher compliance values than their thick-walled counterparts and so are expected to deform more under the same compression. The 1.0 mm thick simulation exhibiting higher strain in the major axis than the 1.5 mm thick simulation is then expected. Consequently, a combination of the silicone model used in practice having thinner walls than an *in vivo* inferior vena cava and slightly different mechanical properties can easily lead to a higher experimental compliance, thus explaining the strain increases from computational to experimental results.

Additionally, both of the simulated models already have reasonably small percent differences in comparison to experimental data, confining accuracy differences to less than 15% across the entire cIVC domain, with the exception of the most severe collapse (75.8% cIVC). Such low variations between the experimental platform and simulations (both 1.5 mm and 1.0 mm thick) alongside agreement with measurements in literature already suggest partial validation of this experimental platform with reason to expect better correlation between experimental and computational results with increased wall thickness in the Sylgard 184 model.

The thorough testing placed on this platform strongly supports the repeatability of these results. Altogether, five trials were performed at each condition, with the flow loop and chamber being deconstructed between each instance to drain the loop. The combined data at each tested condition yielded standard deviations on the order of about 0.5 mm, which, while significant, indicate that

geometric changes can be recreated within a small enough range to produce consistent deformations between trials, even after flow loop reconstruction.

In the overarching context of creating a benchtop setup for further study of IVC filter performance through both mechanical and fluid interactions, this experimental platform shows promise in its ability to recreate the *in vivo* geometry of the infrarenal IVC lumen during localized and dynamic diaphragmatic compression, especially with improvements focused on silicone model geometry. Even more, the applications of this platform can easily be expanded to include any desired effects on the IVC via custom motor control on roller motion, making this a versatile and effective tool for characterizing the relationship between IVC hemodynamics and filter performance.

Section 7.2: Future Work

Because this experimental platform demonstrates a novel way to recreate IVC compression in an accessible model, its value lies in future research. In order to improve the platform itself, a new version of the Sylgard 184 model is needed. At the time of this work, manufacturing limitations restrained silicone model thicknesses to only 1.0 mm, yet a combination of experimental and computational results point towards an increase in silicone wall thickness as the key to adjusting model mechanics to further improve the platform's accuracy. Before this platform is used for other experimental research, more effort should be spent in refining the Sylgard 184 manufacturing process to provide a better compliant model of IVC tissue.

As discussed at length throughout, the hemodynamics surrounding IVC filters play a large role in filter performance, yet no previous studies have taken into account the influence of diaphragmatic motion on the IVC. Because of this, there is a need to study the surrounding flow field while incorporating this effect. The majority of future work with this platform involves performing particle image velocimetry

during roller compression at various physiological states. This imaging will provide new information that could prove valuable in characterizing filter effects on IVC hemodynamics.

BIBLIOGRAPHY

1. What is Pulmonary Embolism? National Heart, Lung, and Blood Institute. https://www.nhlbi.nih.gov/health/health-topics/topics/pe. Published 2011. Accessed October 10, 2017.
2. Douketis JD. Deep Venous Thrombosis. Merck Manual. http://www.merckmanuals.com/professional/cardiovascular-disorders/peripheral-venous-disorders/deep-venous-thrombosis-dvt. Published 2016. Accessed October 10, 2017.
3. Tan M, Mol GC, Van Rooden CJ, et al. Magnetic resonance direct thrombus imaging differentiates acute recurrent ipsilateral deep vein thrombosis from residual thrombosis. *Blood*. 2014;124(4):623-627. doi:10.1182/blood-2014-04-566380.
4. Venous Thromboembolism (Blood Clots). Centers for Disease Control and Prevention. https://www.cdc.gov/ncbddd/dvt/facts.html. Published 2017. Accessed October 10, 2014.
5. Watson T, Shantsila E, Lip GY. Mechanisms of thrombogenesis in atrial fibrillation: Virchow's triad revisited. *Lancet*. 2009;373:155-166. doi:10.1016/S0140-6736(09)60040-4.
6. Thompson GE, Ginsberg JS. Blood Clot in a Vein. Healthwise. https://www.webmd.com/dvt/venous-thrombus. Published 2015. Accessed October 15, 2017.
7. Mackman N. New insights into the mechanisms of venous thrombosis. *J Clin Invest*. 2012;122(7):2331-2336.
8. Stein P. *Pulmonary Embolism*. 2nd ed. Malden, MA: Blackwell Publishing; 2015.

9. Green D. Coagulation cascade. *Hemodial Int*. 2006;10:S2-S4.

10. Silverstein MD, Heit JA, Mohr DN, Petterson TM, Michael O'fallon W, Melton III LJ. Trends in the Incidence of Deep Vein Thrombosis and Pulmonary Embolism. *Arch Intern Med*. 1998;158:585-593.

11. Douketis JD. Chronic Venous Insufficiency and Postphlebitic Syndrome. Merck Manual. http://www.merckmanuals.com/professional/cardiovascular-disorders/peripheral-venous-disorders/chronic-venous-insufficiency-and-postphlebitic-syndrome. Published 2016. Accessed October 11, 2017.

12. Avgerinos E. Pulmonary Embolism. Society for Vascular Surgery. https://vascular.org/patient-resources/vascular-conditions/pulmonary-embolism. Published 2004. Accessed October 12, 2017.

13. Pulmonary Embolism. University of Virginia. https://www.med-ed.virginia.edu/courses/rad/cxr/pathology6chest.html. Published 2013. Accessed October 13, 2017.

14. Carson JL, Kelley MA, Duff A, et al. The Clinical Course of Pulmonary Embolism. *N Engl J Med*. 1992;326:1240-1245. http://www.nejm.org/doi/pdf/10.1056/NEJM199205073261902.

15. K J, M H, H D, et al. Mortality of Patients with Pulmonary Embolism. *Wien Klin Wochenschr*. 2002;114(17-18):766-772. https://www.ncbi.nlm.nih.gov/pubmed/12416281.

16. Meyer G, Planquette B, Sanchez O. Long-term outcome of pulmonary embolism. *Curr Opin Hematol*. 2008;15:499-503.

17. Prandoni P, Lensing AWA, Piccioli A, et al. Recurrent venous thromboembolism and

bleeding complications during anticoagulant treatment in patients with cancer and venous thrombosis. *Blood*. 2002;100(10):3484-3488. doi:10.1182/blood-2002-01-0108.

18. Homans J. Operative Treatment of Venous Thrombosis in the Lower Limbs. *Am J Med*. 1947;3(3):345-354. https://www.sciencedirect.com/science/article/pii/0002934347901654.
19. Lipscomb IP, Nokes LDM. *The Application of Shape Memory Alloys in Medicine*. Loddon, Norfolk: Paston Press; 1996.
20. Mobin-Uddin K, McLean R, Jude JR. A New Catheter Technique for Prevention of Pulmonary Embolism. *Am Surg*. 1969;35:889-894.
21. Jia Z, Wu A, Tam M, Spain J, McKinney JM, Wang W. Caval Penetration by Inferior Vena Cava Filters. *Circulation*. 2015;132:944-952. doi:10.1161/CIRCULATIONAHA.115.016468.
22. Ghatan CE, Ryu RK. Permanent versus Retrievable Inferior Vena Cava Filters: Rethinking the One-Filter-for-All Approach to Mechanical Thromboembolic Prophylaxis. *Semin Intervent Radiol*. 2016;33(2):75-78. doi:10.1055/s-0036-1582123.
23. Chung J, Owen RJT. Using Inferior Vena Cava Filters to Prevent Pulmonary Embolism. *Can Fam Physician*. 2008;54:49-55. https://www.ncbi.nlm.nih.gov/pmc/articles/PMC2293317/pdf/0540049.pdf.
24. Sildiroglu O, Ozer H, Turba UC. Management of the thrombosed filter-bearing inferior vena cava. *Semin Intervent Radiol*. 2012;29(1):57-63. doi:10.1055/s-0032-1302453.
25. Wang S, Siddiqui A, Rosenthal E. Long-term Complications of IVC Filters: Initial Report from the Kaiser Permanente National IVC Filter Registry (KIFR). *J Vasc Interv Radiol*. 2016. doi:10.1016/j.jvir.2015.12.273.
26. Shennib H, Bowles B, Hickle K. Migration of a Fractured Inferior Vena Cava Filter Strut

to the Right Ventricle of the heart: A Case Report. *J Cardiothorac Surg*. 2014;9(183). doi:10.1186/s13019-014-0183-8.

27. Leask RL, Johnston KW, Ojha M. In Vitro Hemodynamic Evaluation of a Simon Nitinol Vena Cava Filter: Possible Explanation of IVC Occlusion. *J Vasc Interv Radiol*. 2001;12(5):613-618. https://www.ncbi.nlm.nih.gov/pubmed/11340141.

28. Couch GG, Johnston KW, Ojha M. An In Vitro Comparison of the Hemodynamics of Two Inferior Vena Cava Filters. *J Vasc Surg*. 2000;31(3):539-549. doi:10.1067/mva.2000.103799.

29. Singer MA, Wang SL. Modeling Blood Flow in a Tilted Inferior Vena Cava Filter: Does Tilt Adversely Affect Hemodynamics? *J Vasc Interv Radiol*. 2011;22(2):229-235. doi:10.1016/j.jvir.2010.09.032.

30. Aycock KI, Campbell RL, Manning KB, et al. A Computational Method for Predicting Inferior Vena Cava Filter Performance on a Patient-Specific Basis. *J Biomech Eng*. 2014;136(8):81003. doi:10.1115/1.4027612.

31. Murphy EH, Johnson ED, Arko FR. Evaluation of Wall Motion and Dynamic Geometry of the Inferior Vena Cava Using Intravascular Ultrasound: **Implications for Future Device Design**. *J Endovasc Ther*. 2008;15(3):349-355. doi:10.1583/08-2424.1.

32. Kimura BJ, Dalugdugan R, Gilcrease GW, Phan JN, Showalter BK, Wolfson T. The effect of breathing manner on inferior vena caval diameter. *Eur J Echocardiogr*. 2011;12(2):120-123. doi:10.1093/ejechocard/jeq157.

33. Gignon L, Sc M, Roger C, et al. Influence of Diaphragmatic Motion on Inferior Vena Cava Diameter Respiratory Variations in Healthy Volunteers. *Anesthesiology*. 2016;124(6):1-9. doi:10.1097/ALN.0000000000001096.

34. Laborda A, Kuo WT, Ioakeim I, et al. Respiratory-Induced Haemodynamic Changes: A Contributing Factor to IVC Filter Penetration. *Cardiovasc Intervent Radiol*. 2015;38:1192-1197. doi:10.1007/s00270-015-1077-4.

35. Tedaldi E, Montanari C, Aycock KI, Sturla F, Redaelli A, Manning KB. An experimental and computational study of the inferior vena cava hemodynamics under respiratory-induced collapse of the infrarenal IVC. *Med Eng Phys*. 2018;54:44-55. doi:10.1016/j.medengphy.2018.02.003.

36. Fox EM. Fluid Dynamic Study of a Compliant Model for an Inferior Vena cava Filter. 2013.

37. Alhosseini Hamedani B, Navidbakhsh M, Ahmadi Tafti H. Comparison between mechanical properties of human saphenous vein and umbilical vein. *Biomed Eng Online*. 2012;11(1):59. doi:10.1186/1475-925X-11-59.

38. Johnston ID, McCluskey DK, Tan CKL, Tracey MC. Mechanical characterization of bulk Sylgard 184 for microfluidics and microengineering. *J Micromechanics Microengineering*. 2014;24(3):35017. doi:10.1088/0960-1317/24/3/035017.

39. Cheng CP, Herfkens RJ, Taylor CA. Inferior vena caval hemodynamics quantified in vivo at rest and during cycling exercise using magnetic resonance imaging. *Am J Physiol Hear Circ Physiol*. 2003;284:H1161-H1167. doi:10.1152/ajpheart.00641.2002.

40. Wade OL. Movements of the thoracic cage and diaphragm in respiration. *J Physiol*. 1954;124(2):193-212. doi:10.1113/jphysiol.1954.sp005099.

41. Silverthorn DU, Johnson BR, Ober WC, Garrison CW, Silverthorn AC. *Human Physiology*. 5th ed. San Francisco, CA: Pearson Benjamin Cummings; 2010.

42. Wang D, Lam A, Poursaid A. Dissection of the Bovine Heart.

43. Laborda A. Influence of breathing movements and Valsalva maneuver on vena caval dynamics. *World J Radiol*. 2014;6(10):833. doi:10.4329/wjr.v6.i10.833.

PHILIP E. CROMPTON

610.952.6257 | pcrompton14908@gmail.com

EDUCATION

The Pennsylvania State University | *Schreyer Honors College* — **University Park, PA**
College of Engineering | B.S. in Biomedical Engineering, Biomechanical Focus — *Graduation May 2018*
College of Engineering | B.S. in Mechanical Engineering

PROFESSIONAL EXPERIENCE

Plexus Engineering Solutions — **Raleigh, NC**
Hardware Design Intern — *May 2017 – Aug 2017*
- Collaborated on a cross-discipline team to integrate mechanical and electrical subsystems in a robotic surgical system, personally including a modular emergency backup power system
- Involved in assembling and working with multiple robotic surgical units
- Coordinated with Plexus' manufacturing division to ensure design manufacturability, especially consider material costs, assembly costs, and general efficiency
- Wrote testing protocols, built prototypes, and carried out testing verifying all mechanical and electrical projects
- Participated in professional development workshops with upper management, learning about managing engineering design projects from a business perspective

Penn State Artificial Heart Lab Summer Research Program — **University Park, PA**
Undergraduate Researcher — *May 2016 – Aug 2016*
- Developed experimental design of mechanical models and software to simulate vascular device situations
- Wrote MATLAB particle tracking scripts for analyzing the motion of a membrane component separating blood and air in the Penn State Pulsatile Pediatric Ventricular Assist Device (PVAD) with the end goal of validating a computation fluid-structure-interaction model
- Designed and machined models to monitor flow characteristics in vascular situations involving recirculation
- Utilized lab protocols to create ghost red blood cells from both human and bovine whole blood for making blood clots that could be chemically and histologically analyzed

PROJECTS & AWARDS

Penn State Artificial Heart Lab — **University Park, PA**
Undergraduate Researcher — *May 2016 – Present*
- Past and Present work on both optical tracking, blood clot analysis, and flow analysis
- Specialty in developing lab protocols and experimental designs centered on physiological problems

Summer Biomechanics, Bioengineering, and Biotransport Conference — **Tucson, AZ**
2nd Place, Undergraduate Student Paper Competition — *Jun 2017*
- "Experimental Motion Tracking of the Membrane in the Penn State Pediatric Ventricular Assist Device"
- Presented personal laboratory research to anonymous judges at a professional conference with over 700 attendees

Evan Pugh Senior Scholar Award (2017) – Academic Excellence | Penn State
President Sparks Award (2016) – Academic Excellence | Penn State
President's Freshman Award (2015) – Academic Excellence | Penn State
Eagle Scout (2014) – Boy Scouts of America

LEADERSHIP & INVOLVEMENT

Penn State IFC Pan-Hellenic Dance MaraTHON — **University Park, PA**
OPPerations Committee, Logistics Captain, THON 2018 — *Sep 2014 – Present*
Volunteer Safety Committee, Alternative Fundraising Captain, THON 2017
- Coordinated all logistics involving transporting materials and setting up/tearing down the event floor during THON weekend in order to create a safe environment for kids undergoing cancer treatment (2018)
- Approved, coordinated, and promoted all alternative fundraising efforts benefitting THON, helping to raise more than $400,000 towards pediatric cancer support at the Hershey Medical Center (2017)
- Each year captain of a committee of 40 students that meet weekly to develop the necessary skills to maintain security and safety or perform setup/teardown and maintenance in the Bryce Jordan Center during THON

RELEVANT SKILLS & COURSEWORK

- MATLAB Scripting and Toolboxes
- Python Scripting and Libraries
- SolidWorks Modeling and Prototyping
- Finite Element Analysis (Theory and Simulation)
- Basic COMSOL Modeling and Simulation
- Microsoft Office Suite
- Cross Cultural International Engineering Seminars
- Engineering Design Methodology
- Laboratory and Workplace Teamwork Skills
- NAUI Confined Water SCUBA Trained